REVIEW

Role of defects in organic–inorganic metal halide perovskite: detection and remediation for solar cell applications

Dinesh Kumar[1] · Shivam Porwal[1] · Trilok Singh[1]

© Qatar University and Springer Nature Switzerland AG 2021

Abstract

Recently, organic–inorganic metal halide perovskite materials have shown great potential for the next generation low-cost renewable energy generation source, and it has surpassed the power conversion efficiency (laboratory scale) of most of the commercially available solar absorbers. Despite the ubiquity and robustness of perovskite materials for defect tolerance in solar cells, its high intrinsic/extrinsic defects remain a bottleneck for real-time application. Thus, a thorough understanding of defect formation and their impact on various recombination losses is a requisite solution for this technology. In this review, we have focused on the formation of various defects and their role in material optoelectronic properties. Further, detailed case studies of each defect via various experimental techniques, their detection and remediation are discussed. Furthermore, the defect detection and remediation approach represent a key step (where optoelectronic properties of the absorber layer can be easily tuned) forward in the sustainable synthesis, fabrication and evaluation of perovskite solar cells.

1 Introduction

Metal halide perovskites (ABX$_3$, where A = MA$^+$ (CH$_3$NH$_3^+$), FA$^+$(HCNH$_2^+$), Cs$^+$, B = Pb^{2+}, Sn^{2+}, X = I$^-$, Br$^-$) have gained a tremendous popularity in a short span for solar cell application after its first use in 2009 by Miyasaka et al. [1] The power conversion efficiency (PCE) has increased from a feeble 3.8 to 25.5% [2] which is close to the state-of-the-art silicon-based solar cells. [3] Unique physical properties such as remarkably high diffusion length [4], high charge carrier mobilities, solution [5] and low temperature processability [6] make perovskite a highly attractive low-cost [7] alternative material compared to the conventional solar cell absorbers such as GaAs, CdTe and crystalline silicon. In order to achieve PCE, close to its Shockley-Queisser limit [8], the underlying physical manifestation of charge carrier defects formed due to the presence of imperfection in perovskite crystals is of utmost need to explore and understand. This review covered the wide variety of physical phenomenon ranging from the defect kinetic, defect dynamics and recombination mechanism. The classification of different type of defects and their kinetics based on the thermodynamic principles is discussed. Secondly, the activation energy of the defect formation in perovskite is discussed based on first principle calculations. Further, various recombination mechanisms due to the presence of defects (non-radiative recombination, radiative recombination and Auger recombination) are discussed in details. Last but not least, we have described the various experimental strategies which are being currently employed for the defect mitigation in perovskite such as the use of material engineering, grain boundary passivation, interfacial engineering and antisolvent vapor-assisted processes.

1.1 Thermodynamic efficiency

Assuming solar cell as a heat converter working between 6000 K (temperature of the sun) and 300 K (ambient temperature). The Carnot efficiency formula (Eq. 1.1) can be applied to calculate the upper power conversion efficiency limit for such a solar converter. [9]

$$\eta = 1 - \frac{T_A}{T_S} \tag{1.1}$$

It is possible to obtain an upper PCE of 95%, but thermal efficiency limit does not consider the entropy-related losses that are dominant inside the solar converter. According to the Kirchhoff law of radiation, any blackbody maintained at

✉ Trilok Singh
  trilok@iitkgp.ac.in

1   Functional Materials and Device Laboratory, School
    of Energy Science and Engineering, Indian Institute
    of Technology Kharagpur, Kharagpur 721302, India

🙂 Springer

thermal equilibrium with surrounding will reemit the radiation with the same rate as it is absorbing. To incorporate these entropy-related losses, one has to incorporate radiation reemission factor from a solar converter maintained at a finite temperature T_C.

In order to consider entropy-related losses for the PCE, blackbody efficiency calculation formula as described in Eq. 1.2 has to be invoked. [9]

$$\eta = 1 - \left(\frac{T_C^4}{T_S^4} - \frac{4T_A}{3T_S} - \frac{4T_A}{3T_C} \times \frac{T_C^4}{T_S^4} \right). \tag{1.2}$$

It is possible to obtain a maximum PCE of 86% when the temperature of a converter is maintained at 2500 K. However, terrestrial-based solar cell absorbers cannot withstand such a high temperature; therefore we need to explore the more practical limit for the absorber material maintained at ambient temperature. One such limit was proposed by Shockley and Queisser in 1961 and famously known Shockley-Queisser limit (SQL) of the PCE. [8] In the next section, we have described about this limit and its consequence on solar cell parameters. This PCE limit is also known as radiative PCE limit of solar cell because authors have only considered radiative recombination as the only mechanism responsible for the charge carrier recombination. Detailed study on the impact of radiative recombination process on perovskite semiconductor physical properties is described in the Sect. 4 of this article.

1.2 Shockley-Queisser efficiency limit

In practical solar cells, we have to consider the impact of the finite bandgap (E_g) of the absorber layer. Shockley and Queisser considered a semiconductor material having a bandgap of E_g with a sharp cutoff frequency (v_g). Since solar cells are essentially a solid state p–n junction diode, authors assumed a unity light absorption coefficient for all the photon frequencies greater than the cutoff frequency of semiconductor. Further, it has been assumed that the radiative recombination is present in the material with single e–h pair generation per single incident photon absorption. Before considering the impact of finite temperature on PCE of solar cell, Shockley and Queisser calculated ultimate PCE for a solar converter maintained ideally at $T=0$ K. The input power incident on solar cell is given by Eq. 1.3. [9]

Incident power $= Ap_s$. where p_s is given by

$$p_s = \frac{2\pi h}{c^2} \int_0^\infty \frac{v^3 dv}{\left(exp\left(\frac{hv}{KT} \right) - 1 \right)} \tag{1.3}$$

p_s is the total amount of radiation incident on solar converter in accordance with Plank's law of radiation, and A is the total device area under consideration. The magnitude of the total output power is given by the relation, output power $= hvA\, q_s$, where q_s is the amount of radiation absorbed by the semiconductor above the cutoff frequency v_g given by Eq. 1.4 [8].

$$q_s = \frac{2\pi}{c^2} \int_{v_g}^\infty \frac{v^2 dv}{\left(exp\left(\frac{hv}{KT} \right) - 1 \right)}. \tag{1.4}$$

Since PCE is the ratio of output power generated by the device divided by the input power incident on the device, so the PCE η is given by Eq. 1.5 [8].

$$\eta = \frac{hv_g q_s A}{Ap_s} \tag{1.5}$$

According to Eq. 1.5, it is possible to obtain a PCE of 44% assuming sun to be maintained at temperature of 6000 K and solar cell to be maintained at 0 K temperature. But this PCE is again not possible because one has to incorporate the finiteness of temperature and also the finiteness of geometrical cross-sectional area of the solar cell. As discussed in the blackbody radiation efficiency limit because of the finite temperature of the solar cell, it is bound to emit radiation in accordance with the Kirchhoff law. In order to calculate steady-state response of the solar cell maintained at finite temperature (300 K), one needs to consider all the dynamical process happening inside the solar cell. Shockley and Queisser identified five such different dynamic processes, and we have defined these different processes as discussed below.

1. Rate of generation of e–h pair due to the absorption of incident photon, and it is denoted by the symbol G_s.
2. Radiative recombination of e–h which will lead to the emission of photons. It is denoted by the symbol $G_c(V)$, where V is the magnitude of quasi-Fermi level splitting due to the incident radiation.
3. Other non-radiative process which leads to generation, and it is denoted by the symbol $R(0)$.
4. Non-radiative recombination of e–h pair due to quasi-Fermi level splitting and it is denoted by the symbol $R(V)$.
5. Removal of photogenerated e–h pair from the active layer which will generate a current density J at the rate of J/q.

For the steady-state response of solar cell: [8]

$$G_S - G_C(V) - R(0) - R(V) - \frac{J}{q} = 0 \tag{1.6}$$

where positive sign is used for the generation of charge carriers in the device, and negative sign is used for removal or recombination of charge carriers out of the device. $R(V)$ and $G(V)$ are related to $R(0)$, $G(0)$ by the relation $R(V) = R(0)exp(V/V_C)$ and $G(V) = G(0)exp(V/V_C)$ respectively. V_C is the thermal voltage equivalent of device operating temperature. On solving Eq. 1.6, steady-state JV response of the solar cell can be obtained, and it is given by Eq. 1.7 [8].

$$J = J_0\left[exp\left(\frac{V}{V_C}\right) - 1\right], J_0 = q(G_C(0) + R(0)) \qquad (1.7)$$

Under light illumination condition, JV response of solar cell is given by Eq. 1.8 [8].

$$J_{rad}|_V = J_0\left[exp\left(\frac{V}{V_C}\right) - 1\right] - J_{Sc} \qquad (1.8)$$

where J_{SC} is the short circuit current density and J_{rad} is the radiative limit of the maximum current at the short circuit condition of the solar cell. In order to obtain open circuit voltage (V_{OC}) of the solar cell, $J=0$ was set inside Eq. 1.8, and the radiative limit for the open circuit voltage is given by Eq. 1.9. [9]

$$J = 0, V_{OC\,rad|} = \frac{KT}{q}ln\left[\left(\frac{J_{SC}}{J_0}\right) + 1\right] \qquad (1.9)$$

In order to get maximum PCE, one has to maximize the product of JV, and the PCE (Eq. 1.10) of a solar cell is given by product of J_{MAX} and V_{MAX} at the maximum voltage condition divided by the amount of incident input power. [8]

$$\frac{dP}{dV} = \frac{d(JV)}{dV} = 0$$

$$\eta = \frac{J_{MAX}V_{MAX}}{P_{inc}} \qquad (1.10)$$

Maximum possible radiative PCE for a single junction solar cell is found to be approximately around 33% with a bandgap of semiconductor in the range 1.2–1.4 eV [8, 9], and the radiative limit for V_{OC} and J_{SC} is defined by Eqs. 1.8 and 1.9 respectively. In order to surpass this efficiency limit, one has to employ the other techniques such as designing a tandem solar cell [10] and hot carrier solar cell [11], but these techniques are beyond the scope of this article. The maximum PCE is a product of the short circuit current and the open circuit voltage. It is possible to increase the V_{OC} of the device simply by increasing the bandgap of the active layer, but at the same time this will hamper the short circuit current of the device since lesser number of photons are now being absorbed inside the active layer. Figure 1a, b, c, d illustrates the variation in PCE, V_{OC}, J_{SC} and FF of a solar cell as a function of semiconductor bandgap. The V_{OC} of a solar cell is observed to be increasing linearly with the increase in the energy bandgap of semiconductor, and J_{SC} is observed to be decreasing with the increase in the energy bandgap of the semiconductor. Since PCE of solar cell is proportional to the product of V_{OC} and J_{SC} of solar cell,

Fig. 1 (a) Variation of Jsc with the change in the bandgap of semiconductor, (b) variation of V_{OC} with the change in the bandgap of semiconductor, (c) variation of FF with the change in the bandgap of semiconductor, (d) variation of PCE due to incident of blackbody spectrum at 6000 K and AM 1.5G spectrum with the change in the bandgap of semiconductor [9]
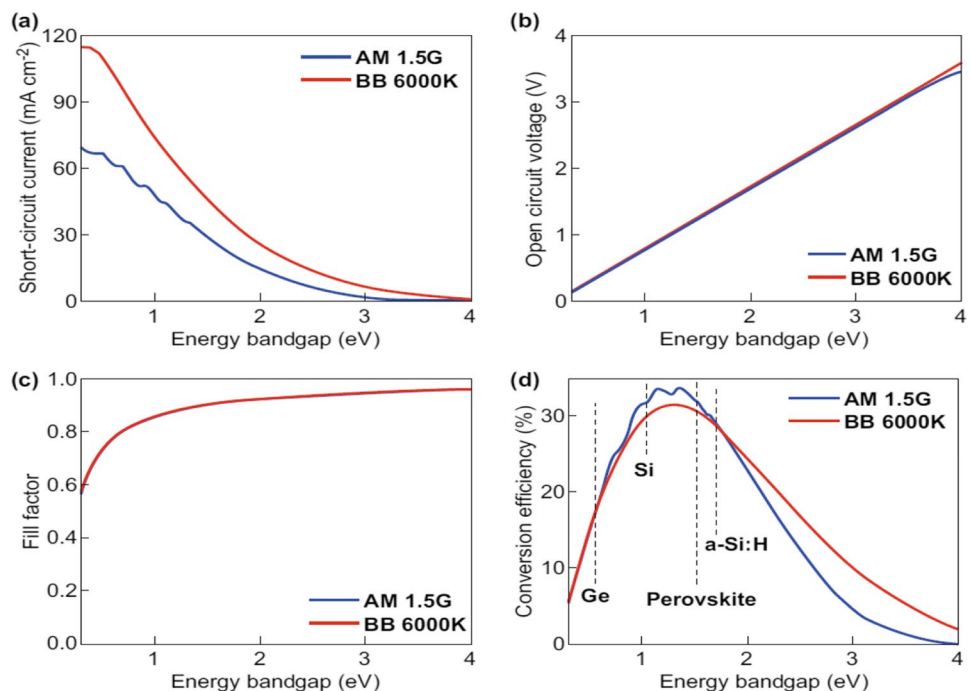
hence firstly it is observed to increase with the increase in the bandgap and then decreases before peaking in the energy bandgap regime 1.2–1.4 eV. These values of various solar cell parameters are only based on the radiative recombination; therefore, one has to consider the other recombination mechanisms as well to explain the observed results of solar cell various parameters.

1.3 Recombination processes in semiconductors

Different recombination processes hinder the upper PCE limit, as SQL takes into consideration only radiative recombination process. Due to the presence of various other recombination mechanisms in the semiconductor, achieving SQL is difficult. In this section, we have described fundamental of different recombination pathways, experimental techniques and few of the case studies in order to develop a deeper understanding about recombination in perovskite-based semiconductors. Semiconductor recombination processes are divided into three categories namely radiative recombination (bimolecular), non-radiative recombination (monomolecular) and Auger recombination. These are the relaxation processes of free charge carriers in the semiconductor material after it is being subjected to external perturbation such as light irradiation or voltage. After the radiative recombination relaxation process, semiconductor will emit a radiation (photon) out of the system, and the magnitude of the recombination process depends upon the product of electron and hole concentration. While the other two recombination processes are non-radiative in nature and relax through emission of phonons inside the material. The rate of monomolecular recombination is directly proportional to the density of trap states (N_T) present in the material, while Auger recombination is a three-particle phenomenon as discussed in more detail in the latter section. All three different processes have different rate constant and hence different time scale of charge carrier's relaxation. Charge carrier lifetime in a semiconductor due to the presence of different recombination processes is given by Eq. 1.11 [12].

$$\frac{1}{\tau_{eff}} = \frac{1}{\tau_{NR}} + \frac{1}{\tau_R} + \frac{1}{\tau_A} \tag{1.11}$$

where τ_{eff} is the effective bulk lifetime of charge carriers and $\tau_{NR}, \tau_A, \tau_R$ are the charge carrier lifetime dictated by the non-radiative, Auger and radiative recombination processes respectively. The rate equation of photogenerated charge carrier decay can be written as Eq. 1.12 [13].

$$\frac{dn}{dt} = -\left(k_1 n + k_2 n^2 + k_3 n^3\right) = -nR \tag{1.12}$$

where K_1, K_2, K_3 are the rate constants for the non-radiative, radiative and Auger charge carrier recombination processes respectively and R is known as the total recombination rate of the device. The effective lifetime of charge carrier can also be written as described below in Eq. 1.13 [14].

$$\tau_{eff} = \frac{\Delta n}{R} \tag{1.13}$$

Δn is the photo-induced charge carrier excitation density. By combining Eqs. 1.12 and 1.13, the charge carrier lifetime for individual recombination process can be written as $\tau_{NR} = 1/K_1$, $\tau_R = 1/nK_2$, $\tau_A = 1/n^2 K_3$. With any semiconducting material having simultaneous presence of all three different recombination processes at certain experimental condition, the process with the lowest amount of lifetime will dominate the overall recombination.

Typically, microcrystalline thin films such as perovskite have defect density in the range of $10^{14}/\text{cm}^3$ to $10^{17}/\text{cm}^3$ [15]. Hence, if the incident photon density lies in this range, usually the monomolecular recombination process starts to dominate. At the incident photon density comparable or higher than the $10^{17}/\text{cm}^3$, the monomolecular recombination channel will saturate and the bimolecular recombination starts to dominate in the semiconductor (Fig. 2). For higher incident photon densities, bimolecular recombination channel alongside monomolecular also saturates and Auger recombination becomes the dominate recombination process.

1.4 Monomolecular recombination

K_1 is known as the rate constant for non-radiative recombination process of the semiconductor material. The source of non-radiative recombination is the deep lying defect energy states present inside the bandgap of a semiconductor. These defect energy level can arise due to the presence of various defects such as point defects, surface states (dangling bonds), grain boundaries and other dislocations. The mathematical model to define non-radiative recombination in the semiconductor is given by Shockley, Read and Hall (SRH recombination model). [14] This is the statistics model of non-radiative recombination mechanism happening in a semiconductor material due to the presence of single defect level inside the semiconductor bandgap at the energy level location E_T with the defect density N_T. Four different recombination processes such as R_1 being the rate of electron capture by the traps, R_2 is the rate of electron emission by the traps and R_3 and R_4 being the hole emission and capture rates due to the traps dominate respectively. At thermal equilibrium condition, the net recombination rate of electron capture and emission must be equal to the net rate of capture and emission of holes as given by Eq. 1.14 [14].

$$R = R_1 - R_2 = R_3 - R_4 \tag{1.14}$$
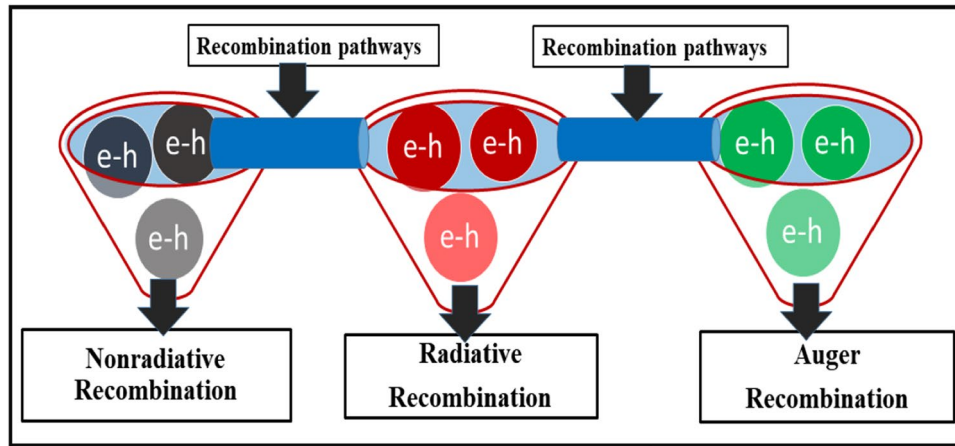
Fig. 2 *'The Bucket analogy'*: This is the illustration of the dominance of one type of recombination process over the other type of recombination process in typical microcrystalline perovskite-based thin films. We have denoted three recombination processes by the three different buckets of water (water ~ photogenerated charge carriers) since three buckets are connected in series by a connector (~ recombination pathways) at the top of each bucket. In case of perovskite thin films, only if the bucket 1 (~ non-radiative recombination center) is completely filled (or saturated) water will pass through into bucket 2 (~ radiative recombination), and only if bucket 2 is filled water will pass through in the bucket three (~ Auger recombination)

The rate of overall recombination due to the presence of a single defect inside the semiconductor bandgap is given by Eq. 1.15 [16, 17].

$$R = \frac{N_T V_{th} \sigma \left(np - n_i^2\right)}{\left(n + p + 2n_i \text{Cosh}(\frac{E_t - E_i}{KT})\right)} \tag{1.15}$$

where V_{th} is the thermal velocity, σ is the cross-section area, n_i and E_i are the intrinsic carrier concentration and intrinsic energy location of the bandgap respectively. The rate of recombination is observed to be maximum whenever $E_t = E_i$, i.e. if the trap level is located in the middle of the semiconductor bandgap and such trap levels are also known as deep level traps. As the trap levels moves away from the middle of the bandgap and towards the conduction band or valance band edges, the non-radiative recombination rate starts to decrease; such defect levels are also known as shallow defect levels. The SRH lifetime of charge carrier is given by the relation $\tau_{SRH} = \left(v_{th} \sigma N_T\right)^{-1}$.

1.5 Radiative recombination

As discussed earlier in the rate Eq. 1.12, K_2 is known as the bimolecular radiative recombination coefficient. Whenever charge carriers from the top of conduction band recombine with the bottom of the valance band, radiation is emitted in the form of photons. Using the optical reciprocity relation radiative recombination coefficient, K_2 can be calculated as shown below in Eq. 1.16. [18]

$$K_2 = \frac{\int_0^\infty 4\alpha(E) n_r^2 \phi_{bb} dE}{n_i^2} \tag{1.16}$$

$\alpha(E), n_{(r)}$ are the light absorption coefficient and refractive index of the semiconductor material, and ϕ_{BB} is the incident solar flux given by the Plank's law of radiation, and it is given by Eq. 1.17 [18].

$$\phi_{bb}(E) = \frac{2\pi E^2}{h^3 C^2} \left[\frac{1}{exp\left(\frac{E}{KT} - 1\right)} \right] \tag{1.17}$$

By the principal of optical reciprocity, any good absorbing semiconductor material is also a very good radiation emitter. Because radiative recombination pathways are the same as light absorption pathways, but this is not true in case of the nonradiative recombination pathways [19]. A good quality solar cell should emit radiation as much as it absorbs under the open circuit voltage condition. [19–21] As described earlier, radiative recombination is a two particle pheonemenon; hence, the total recombination rate will depend upon the product of the elecrons and holes, and its expression is given by Eq. 1.18 [18].

$$R = K_2 np = K^2 n_i^2 exp\left(\frac{\Delta E_F}{KT}\right) \tag{1.18}$$

1.6 Auger recombination

Auger recombination is a third-order recombination process widely observed in different semiconductors. It is three particle phenomena where after the initial radiative recombination

of photogenerated charge carrier, the emitted photon is again re-absorbed by an electron or hole. After absorbing the photon, electrons in the conduction (holes in valance band) band become a hot electron and relax back to thermal equilibrium by emitting the multiple phonons. Such a process is also known as the impact ionization of charge carriers. Auger recombination is also a non-radiative process in nature. Auger recombination can be divided into multiple types, and the various recombination rates are listed below in Eq. 1.19. [22] Auger recombination can also process through reabsorption of emitted photon due to the trap level present inside the bandgap. Typical Auger recombination rate is given as

$$
\left.\begin{array}{l}
R_{aug} = K_3 n^2 p \\
R_{aug} = K_3 n p^2 \\
R_{aug} = K_3 n p N_T
\end{array}\right\}. \tag{1.19}
$$

K_3 is the Auger recombination rate constant. By neglecting the Auger recombination due to trap states and using Eq. 1.19, total Auger recombination can be written as [22]

$$
R_{aug} = K_3 n^2 p + K_3 p^2 n. \tag{1.20}
$$

By assuming $n = p$ which holds very much true for an intrinsic semiconductor such as a perovskite, Eq. 1.20 can be rewritten as [22]

$$
R_{aug} \propto K_3 n^3. \tag{1.21}
$$

Using the relation $np = n_i^2 exp\left(\frac{qV}{KT}\right)$ [17] and substituting in Eq. 1.21 [22], the Auger recombination rate can be written as

$$
R_{aug} \propto K_3 n_i^3 exp\left(\frac{qV}{3KT}\right). \tag{1.22}
$$

Auger recombination typically dominates in the carrier density regime of 100 s order magnitude higher than the usual operating condition of the solar cell, so for the terrestrial thin film-based solar cell Auger recombination is a negligible phenomenon. Auger recombination plays a vital role under large illumination injection and at high doping density levels. [22] Detailed study of Auger recombination using SRH like statistics model can be found in a study recently published by Staub et al. [23].

2 Defects type, kinetics and their formation energy in perovskite semiconductors

2.1 Defects in perovskite

Defect formation in materials is inevitable in nature because solidification always takes place at finite temperature (> 0 K). The presence of imperfections strongly influences

the properties of materials; thus, to understand their role in the physical parameter alternation is highly important. [24–26] Crystalline defects are simply defined as the lattice irregularity at the atomic scale in one or more than one dimensions, and such defects are classified mainly into four different categories namely zero-dimensional point defects and extended dimensional defects such as one dimensional (screw and edge dislocation), two dimensional (stacking faults, grain boundaries) and three-dimensional defects such as aggregation of the impurities. Defects modify the electronic structure of semiconductor by introducing the energy level inside the bandgap of semiconductor. The optoelectronic properties of semiconductor material are highly influenced by the type of defect present in the semiconductor material and the energy states created by the defects [27]. The carrier diffusion length and charge carrier lifetime of solar cell absorber are important parameters for determining the quality of solar cells, and these two parameters are highly influenced by the type of defects present inside the material. [28] Shallow level point defects are observed to have low formation energy in MAPbI$_3$-based perovskite, while deep level defects are observed to have high formation energy. [29, 30] Halide perovskite-based semiconductors possess a massive number of intrinsic point defects, and it is very important to understand the thermodynamic stability, intrinsic point defect formation mechanism and the kinetics of defect formation in halide perovskites.

2.2 Kinetics of defect formation

Yin et al. studied the defects in MAPbI$_3$ and predicted that the defect formation energies dominantly create shallow level states inside the bandgap of MAPbI$_3$. [30] The defect study suggests that Pb^{2+}, MA$^+$, I$^-$ create shallow donor and acceptor level states as described below in Fig. 3. In general, perovskite material is observed to show the formation 12 types of point defects. Three vacant point defects correspond to the missing MA$^+$, Pb^{2+}, I$^-$ ions from their respective lattice sites and are denoted by the symbol V_{MA}, V_{Pb}, V_I respectively. The migration of MA$^+$, Pb^{2+}, I$^-$ to the interstitial site denoted by the symbol MA$_i$, Pb$_i$, I$_i$ respectively is observed to cause interstitial point defects. The substitution of cations by the anions such as MA$_I$, I$_{MA}$, Pb$_I$ and I$_{Pb}$ is known as the antisite point defects, while MA$_{Pb}$ and Pb$_{MA}$ are known as the substitutional point defects.

Defect formation energy in MAPbI$_3$ was derived by Walsh et al. [32] using the Kröger and Vink notations as described below in Eqs. 2.1–2.3. Authors have considered the reaction of partial and full Schottky disorder with respect to MAI and PbI$_2$ sub lattices.

Partial Schottky disorder reaction is given by Eqs. 2.1 and 2.2 [32].

Fig. 3 Schematics of energy
levels associated with the vari-
ous defect states vacancies (V_{Pb},
V_I, V_{MA}), neutral and charged
interstitials (Pb_i, I_i, MA_i), states
associated with antisites (Pb_I
and I_{Pb}) present inside the band-
gap of MAPbI$_3$ calculated using
the first principle analysis [31]

$$Nil \rightarrow V'_{MA} + V°_I + MAI \qquad (2.1)$$

$$Nil \rightarrow V''_{Pb} + 2V°_I + PbI_2 \qquad (2.2)$$
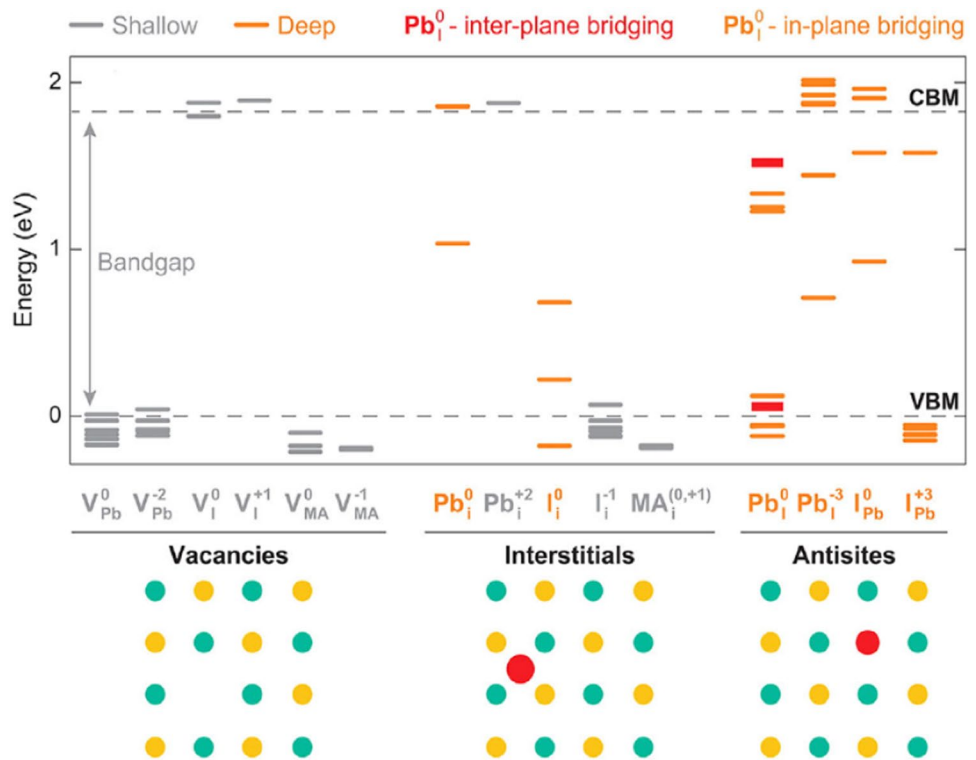
Full Schottky disorder reaction is given by Eq. 2.3 [32].

$$Nil \rightarrow V'_{MA} + V''_{Pb} + 3V°_I + MAPbI_3 \qquad (2.3)$$

where Nil represents the ordered MAPbI$_3$ lattice, V'' is the
vacant site due to the missing divalent cation and V', V^0
represent the missing vacant site due to monovalent cation,
vacancy due to the missing halide anion respectively. The
ionic species and effective defect charges are represented in
subscript and superscript respectively. Reaction 3 preserves
the overall stoichiometry ratio within the material, and reac-
tions 1, 2 are non-stoichiometric in nature. Since due to high
atomic radius of halide ions, there is not enough interstitial
space available for halide ions to migrate interstitial so I^-,
Pb^{2+} and MA^+ vacancy mediated diffusion is the most com-
mon defect reaction observed in the perovskite semiconduc-
tors. The three-vacancy transport mechanism reported by
Eames et al. [33] is based on the hopping of ions between the
neighboring positions such as the migration of Pb^{+2} within
the cubic unit cell along the diagonal direction $<110>$,
migration of I^- along the octahedral edge and the migration
of MA^+ into the vacant A site position. The equilibrium

concentration can be calculated thermodynamically using
the law of mass action given by Eq. 2.4 [32].

$$\left[V'_{MA}\right]\left[V^ε_{Pb}\right]\left[V°_I\right]^3 = K_C = K_C° exp\left(-\frac{\Delta H_S}{KT}\right) \qquad (2.4)$$

where K_C is the fraction of the lattice sites and $K_C°$ are the
vacant sites due to the reaction enthalpy (ΔH_S). The stoi-
chiometric of MAPbI$_3$ phase can be controlled by the growth
conditions because the dissociation energy of this perovskite
to MAI and PbI$_2$ is very low value at 0.27 eV.

2.3 Defects and their formation energy

The second phase formation due to change of temperature
in the perovskite is avoided by controlling the growth condi-
tion of MAPbI$_3$ within the thermodynamically stable nar-
row chemical potential region. The chemical potential is
corresponding to the energy of point defect formation. The
dominant point defects in MAPbI$_3$ are MA_I and V_{Pb}. The
chemical potential energy for the ion migration of MAPbI$_3$
can be calculated from the following set of Eq. 2.5 [30].

$$\left.\begin{array}{r} \mu_{CH_3NH_3} + \mu_{Pb} + 3\mu_I = \Delta H_S\left(CH_3NH_3PbI_3\right) = -5.26eV \\ \mu_{CH_3NH_3} + \mu_I < \Delta H_S\left(CH_3NH_3I\right) = -2.87eV \\ \mu_{Pb} + 2\mu_I < \Delta H_S\left(PbI_2\right) = -2.11eV \end{array}\right\}$$

$$(2.5)$$

The MA$^+$ cation is non-centrosymmetric, and Yin et al. [30] also found that the total energy and electronic structure of MAPbI$_3$ are fragile because of weak Van der Waals interaction between oriented non-centrosymmetric MA$^+$ and 3-D Pb-I framework. Yin et al. [30] also reported the relationship between chemical potential (μ) of constituent elements and their defect formation enthalpy (ΔH_S). This study considered all possible point defects including three vacant sites ($V'_{MA}, V''_{Pb}, V°_I$), all interstitial ($MA_i^°, Pb_i, I_i\ MA_i^°, Pb_i, I_i$), the substitution of cations (MA_{Pb}, Pb_{MA}) and antisite substitutions (MA_I, Pb_I, I_{MA}, I_{Pb}). These defects also contribute towards the conduction mechanism in halide perovskite, which is important to understand the unusual ionic conduction in perovskites. This study also revealed that an unusual behavior such as current–voltage hysteresis and dielectric response observed at low frequency is mainly due to the migration of ions, so halide perovskites are the mixed ionic-electronic conductors.

The defect formation energy is shown in the Table 1. The defects such as MA$_i$, V_{Pb}, MA$_{Pb}$, I$_i$, V_I and V_{MA} having formation energy less than ~ 0.5 eV are observed near the valance band or the conduction band edge of MAPbI$_3$. Thus, these defects are observed to create only shallow level states in between the bandgap and other defects such as I$_{PB}$, I$_{MA}$, Pb$_i$, Pb$_I$ having high formation energy, which creates deep defect level states. The defects such as V_{Pb} and MA$_{Pb}$ are dominant vacancies for shallow level states, which originates from the antibonding states present at valance band maximum (VBM). The shallower nature of MA$_i$ and V_I is observed mainly due to the high ionic nature of MA and Pb ions. The most common defects in MAPbI$_3$ have been reported as p-type V_{Pb} and n-type MA$_i$ which are mainly responsible for recombination and ionic conduction in MAPbI$_3$-based solar cells. This study indicated that the halide perovskites may not be in the pure perovskite phase, whereas the second phase may arise due to the formation of defects by the low formation energies. Impact of defects on solar cell performance parameters, the fundamental efficiency limitation of solar cell and efficiency limitation due to the presence of various recombination processes caused by the various defects in perovskite is already discussed in the previous section.

2.4 Factors effecting non-radiative recombination-shallow and deep level defects

Shallow level trap states are the states which lie very near to the conduction or valance band edge of the semiconductor. These states can be easily ionizable at room temperature and contribute towards conduction in semiconductors. One such example is of doped semiconductor, where acceptor or donor levels are shallow level states. According to SRH recombination model [14], theses states do not contribute much towards the non-radiative recombination. Usually dangling bonds present due to surface termination cause deep level traps in the semiconductor. Since trap states below the intrinsic Fermi level of semiconductor are occupied with the free charge carriers. So due to the presence of large occupied trap states while forming a metal semiconductor contact, sometimes a thermal equilibrium condition can be established between the surface states of a semiconductor and metal contact of the solar cell. In such cases, the thermal equilibrium between the semiconductor band edges and metal contact is hindered, and this situation is also known as Fermi level pinning of the absorber layer of a solar cell. [35] The presence of deep level traps highly impacts the open circuit voltage of the solar cell because of ineffective quasi-Fermi splitting due to the presence of Fermi level pinning. Another example of deep lying states in perovskite-based solar cell is the diffusion of metal contact cation inside the active semiconductor layer. [36] In order to overcome these challenges, one has to detect, mitigate and passivate these deep level defect states present in the semiconductor bandgap. We have discussed various defect mitigation strategies of perovskite-based solar cell in the Sect. 5 of this review.

3 Defect identification and their influence on physical parameters of perovskite

3.1 Dark JV measurement

JV measurement of solar cell is a great tool for qualitatively determining the impact of defect recombination in the solar cell. Dark *JV* response of the solar is similar to solid-state diode and is given by Eq. 3.1 [37], J_{rad} is the radiative current density of the solar cell.

Table 1 Defect formation energies (eV) of various point defects in MAPbI$_3$ perovskite calculated using the first principle method [34]

Condition	I$_i$	MA$_{Pb}$	V$_{MA}$	V$_{Pb}$	I$_{MA}$	I$_{Pb}$	MA$_i$	Pb$_{MA}$	V$_I$	Pb$_i$	MA$_I$	Pb$_I$
Pb-rich/I-poor	0.23	0.28	0.81	0.29	1.96	1.53	1.39	2.93	1.87	4.24	3.31	5.54
Moderate	0.83	1.15	1.28	1.62	3.01	3.45	0.93	2.51	1.27	2.91	2.25	3.62
Pb-poor/I-rich	1.42	1.47	2.01	2.68	4.34	5.10	0.20	1.74	0.67	1.85	0.93	1.97

$$J_{rad}(V) = J_0 \left[exp\left(\frac{qV}{KT} \right) - 1 \right] \tag{3.1}$$

Due to the presence of other non-radiative recombination centers, the dark JV response of solar cell has to be modified by a factor as shown below in Eq. 3.2. [38]

$$J_{non-rad}(V) = J_0 \left[exp\left(\frac{qV}{nKT} \right) - 1 \right] \tag{3.2}$$

where n is known as diode quality factor. Slope of $ln(J)$ vs V (Eq. 3.3) [38] in the small voltage regime ($V < V_{bi}$) can be used to estimate the diode quality factor. Figure 4b indicates the estimation of diode quality factor using the dark JV response of MAPbI$_3$-based solar cell.

$$n = \left[\left(\frac{KT}{q} \frac{\partial ln(J)}{\partial V} \right) \right]^{-1} \tag{3.3}$$

By comparing Eqs. 3.1 and 3.2, it can be seen that the diode quality factor for radiative recombination mechanism is unity. Usually due to the presence of various non-radiative recombination centers, diode quality factor of a solar cell usually lies between 1 and 2. [38, 39] Whenever the value of diode quality factor is unity, then the transport in solar cell is of purely diffusive nature, and transport is limited by the space charge region. For diode quality factor value $n > 1$, transport is governed by both diffusion and drift of charge carriers. Depending upon the type of recombination, the radiative current of solar cell scale as $J_{rad} \propto n^\alpha$ where diode quality factor n and α related by the relation $n = 2/\alpha$,

$\alpha = 1$ for pure non-radiative recombination, and $\alpha = 2$ for the pure radiative recombination. [40]

3.2 CV profiling

Capacitance of p–n junction arises due to the diffusion of majority charge carriers from n to p side and p to n side of the junction because of the presence in diffusion gradient on both sides. Due to the diffusion of charge carriers, p–n junction becomes depleted of majority charge carrier (electron on n side of the semiconductor and holes on p side of the semiconductor), and this region of depletion is also known as space charge region of the diode and width of region is known as depletion width of the diode. Capacitance measurement of p–n junction is sensitive to charge carrier capture and emission due to the defect states present inside the bandgap. Small signal variation in differential capacitance ($C = \frac{dq}{dV}$) can furnish the information about the orientation and influence of sub bandgap states on the non-radiative recombination in semiconductors. These signals mainly originated from space charge region near p–n junction of the diode. Under depletion approximation (abrupt boundaries and fully depleted space charge region), junction capacitance per unit area can be defined by Eq. 3.4 [17].

$$C = \frac{\varepsilon \varepsilon_0}{W} \tag{3.4}$$

where C is the capacitance of junction, ε is dielectric constant, ε_0 is the permittivity of free space and W is the width of depletion region and given by Eq. 3.5 [17].
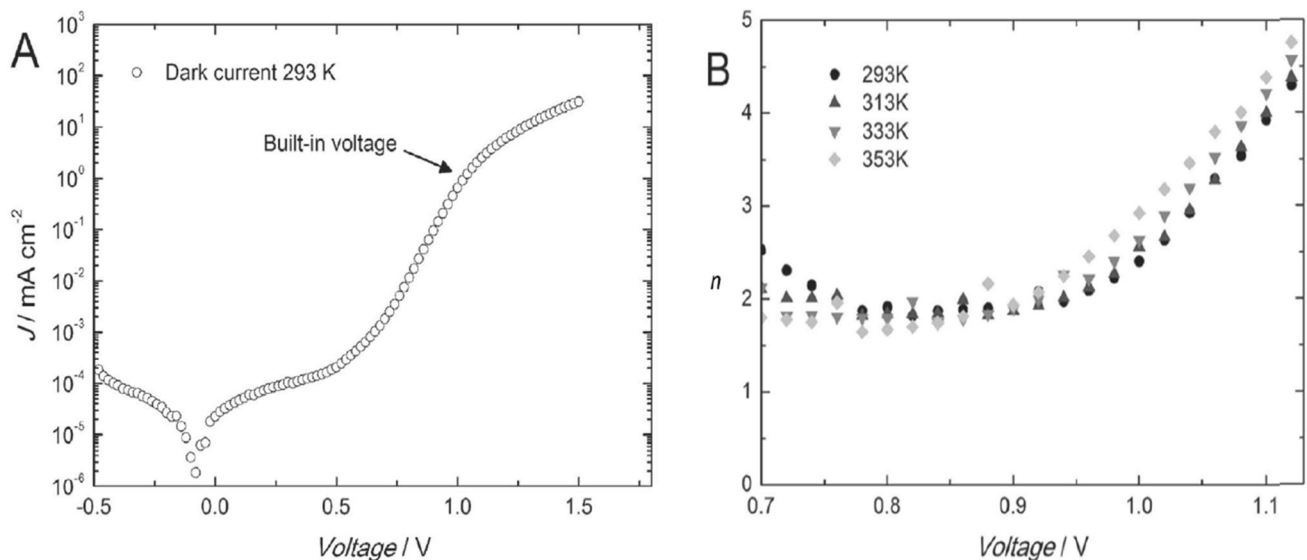
Fig. 4 **(a)** Dark JV response of perovskite-based solar cell in the device stack (PCBM/MAPbI$_3$/polyTPD/PEDOT:PSS/ITO/Substrate), **(b)** determination of temperature dependent diode quality factor by using Eq. 3.3 and using the plateau value of n vs V graph.

The obtained value of diode quality factor was between 1.7 and 1.8 indicating the presence of strong trap-assisted recombination in the device [38]

$$W = \sqrt{\frac{2\varepsilon\varepsilon_0\left(V_{bi} - V_{dc}\right)}{eN_B}} \qquad (3.5)$$

N_B is the doping concentration, V_{bi} is the built-in voltage and V_{dc} is the DC component of applied voltage across the device. By substituting W and replacing $N_B = N_{CV}$ (as N_{CV} is the CV density of states) into Eq. 3.4, the capacitance of junction as a function of applied voltage is given by the Mott-Schottky relation as shown below in Eq. 3.6 [41].

$$C^{-2} = \frac{2\left(V_{bi} - V_{dc}\right)}{e\varepsilon\varepsilon_0 A^2 N_{CV}} \qquad (3.6)$$

Using Eq. 3.6 in a linear scale plot of C^{-2} vs V, the intercept will yield the built-in voltage, and slope will give the estimation Ncv of the device. Under the applied periodic voltage trap states can modify the capacitance of p–n junction diode via modification of space charge density and influencing the depletion width of the diode. Secondly, since trap states are electrically charged, so in the response of external voltage these states can change their charge state behavior dynamically. In order to get response from trap states, the rate of electron capture or emission should be comparable to the input periodic applied voltage frequency ($e_n \sim \omega$). In general, Eq. 3.4 [42] can be modified to the capacitance of the diode.

$$C = \frac{\varepsilon\varepsilon_0 A}{\langle x \rangle} \qquad (3.7)$$

where $<x>$ is the first moment of charge response due to the presence of traps states in the device. [41] The CV response of the device is mainly used to estimate the doping profile, electric field profile, built-in voltage, dielectric constant and the interface quality of the p–n junction diode. [43, 44]

Case studies Using the CV spectroscopic measurements, Guerrero et al. [45] studied the degradation of perovskite solar cell in the device stack ITO/PEDOT:PSS/MAPbI$_3$/PCBM/Metal by varying the metal electrodes as Ca, Ag, Au, Al, Cr$_2$O$_3$-Cr. Authors have observed device with Cr$_2$O$_3$-Cr (buffer layer) as a metal contact showed no S shape JV behavior after the device degradation under constant light illumination. Through CV measurement, authors have compared the bulk properties of perovskite devices before and after the light-induced degradation and concluded that bulk properties of perovskites were not modified significantly before and after the light degradation. But it is the surface states of perovskite/metal interface causing the high detrimental effects. Due to the light-induced dipoles caused by the high charge carrier accumulation region around the metal/perovskite interface, the S shape behavior was observed in the JV response

of the different devices. A buffer layer in-between perovskite and metal could prevent the light-induced dipoles at the metal/perovskite surface. The CV density of states and V_{bi} calculated using CV measurement techniques for some of the devices studied in the literature are listed below in Table 2.

3.3 Deep level transient spectroscopy (DLTS)

DLTS is a measurement of transient capacitance signal generated due to deep lying traps in response to the applied voltage or optical pulse (OD-DLTS). DLTS spectroscopy technique can be used to determine defect type, activation energy, trap concentration and various other parameters such as capture cross-sectional area, location of deep lying states. DLTS signal is calculated using the small change in capacitance value due to the small variation in trap containing charges at the immediate location away from the junction (at $x = 0$) in response to the applied input. The relative DLTS signal is given by Eq. 3.8. [41]

$$\frac{\Delta C}{C} = \frac{N_T \Delta x}{W^2}\left(\frac{x + W_n}{N^-} - \frac{W_p - x}{N^+}\right) \qquad (3.8)$$

N^- and N^+ are the densities of the negatively and positively charged ionized traps on either side of the junction in response to the applied input on the device. N_T is the density of trap states, and Δx is the small positional variation of trap states away from the junction at $x = 0$. Also, C is the imaginary part (Eq. 3.12) of admittance (Z) of p–n junction, and it is given by Eq. 3.9. [41]

$$C = Img\frac{(1/Z)}{\omega} \qquad (3.9)$$

DLTS signal is measured using the probe signal (optical/electrical) on a reversed (forward) biased p–n junction. To observe the capacitance transient of a p–n junction using the DLTS spectroscopy since the p–n junction is reversed biased and immediately after the application of probe pulse, the depletion width of the junction is reduced from its reverse bias condition for a small pulse period of time Δt. Newly generated charge carrier due to the pulse signal is captured by the traps, and after a time Δt when the reverse bias condition of the junction is restored, trap captured minority carrier is swept away, but the captured majority carriers still remain trapped inside the defect states. This leads to a temporary decrease in the capacitance value because of an increase in the depletion width of a p–n junction due to the pulse signal. The small variation in capacitance ΔC is observed as a capacitance transient of the device. Capacitance transition response of the junction is given by Eq. 3.10. [41, 51]

Table 2 Determination of perovskite effective doping density of states (N_{CV}) and built-in voltage (V_{bi}) using *CV* spectroscopic technique

Device architecture	Effective doping density N_{cv} (1/cm³)	V_{bi} (eV)	Reference
FTO/TiO$_2$/MAPbI$_{3-x}$Cl$_x$/Spiro-OMeTAD/Au	18×10^{16}	1.10	[44]
FTO/TiO$_2$/MAPbI$_{3-x}$Cl$_x$/Au	3.2×10^{16}	0.94	[44]
ITO/PEDOT:PSS/MAPbI$_3$/PCBM/Metal	1×10^{16}	1.10	[45]
ITO/PEDOT:PSS/MA(PbI$_2$)$_{1-X}$(CuBr$_2$)$_X$/PCBM/LiF/Al, for $X = 0.1$	9.28×10^{16}	-	[43]
Au/BCP/PCBM/MAPbI$_3$/PEDOT:PSS/FTO	6.93×10^{14}	-	[43]
FTO/TiO$_2$/Perovskite/P3HT/Au	3×10^{16}	-	[46]
FTO/c-TiO$_2$/m-TiO$_2$/MAPbI$_3$/Spiro-OMeTAD /Au	1.4×10^{18}	1.2	[47]
FTO/c-TiO$_2$/ MAPbI$_3$/ Spiro-OMeTAD/Au	2.4×10^{17}	1.2	[47]
FTO/PCBM/C$_{60}$/MAPbI$_3$/PTAA/BCP/Au	2.8×10^{16}	1.0	[48]
FTO/PCBM/C$_{60}$/FAPbI$_3$/PTAA/BCP/Au	2.5×10^{16}	1.3	[48]
FTO/MAPbI$_3$/Au	2.7×10^{14}	-	[49]
FTO/c-TiO$_2$/ m-TiO$_2$/MAPbI$_3$/Spiro-OMeTAD/Au	$(1.37 \times 10^{17})_{peak}$	0.69	[49]
FTO/c-TiO$_2$/m-TiO$_2$/(MAPbI$_3$)$_{0.85}$(FAPbBr$_3$)$_{0.15}$/Spiro-OMeTAD/Au	$(8.84 \times 10^{16})_{peak}$	1.05	[49]
FTO/b-TiO$_2$/m-TiO$_2$/MAPbI$_3$/Spiro-OMeTAD/Au	6.08×10^{17}	0.75	[50]
FTO/b-TiO$_2$/m-TiO$_2$/MAPbI$_3$/MIC2/Spiro-OMeTAD/Au MIC2 = N-methyl thiazolium iodide	1×10^{17}		[50]
FTO/b-TiO$_2$/m-TiO$_2$/MAPbI$_3$/MIC3/Spiro-OMeTAD/Au MIC3 = 3,4-dimethyl thiazolium iodide	7.54×10^{17}	1.18	[50]
FTO/b-TiO$_2$/m-TiO$_2$/MAPbI$_3$/MIC4/Spiro-OMeTAD/Au MIC4 = 3,4,5-trimethyl thiazolium iodide	6.08×10^{17}	1.14	[50]

$$C(t) = C_\infty \left(1 \mp \frac{N_T}{2N^-} exp(-e_t t) \right) \qquad (3.10)$$

$C_{(\infty)}$ is the steady-state capacitance of the *p–n* junction and e_t is the rate of trap capture coefficient by the defect states. The positive sign indicates enhancement in the capacitance, and negative sign indicates decrease in the capacitance value. Capacitance value changes due to the response of trap states before and after the application of input pulse. Rate window for the DLTS signal measurement is defined by Eq. 3.11. [41]

$$\tau = \frac{\tau_1 - \tau_2}{ln(t_1/t_2)} \qquad (3.11)$$

The probing frequency for DLTS is chosen such that $f = \frac{1}{2\pi\tau}$.

Case studies Heo et al. [52] studied the DLTS spectroscopy on single step deposited and double step deposited device based on the MAPbI$_3$ perovskite. Authors have observed two signature defect peaks at the energy location E_1 and E_2 in both devices, but the single step deposited film is observed to be having higher defect density than the double step deposited sample (Table 3). Based on the first principle calculation performed previously [34], authors have assigned 0.60 and 0.75 trap states as substitutional vacancies

of I_{Pb} and I_{MA}. Due to the large defect density in single step deposited device, its Fermi level is likely to be pinned at the center. Polyakov et al. [53] studied mixed cation perovskite Cs$_x$(MA$_{0.17}$FA$_{0.83}$)$_{(1-x)}$Pb(I$_{0.83}$Br$_{0.17}$)$_3$ using the DLTS spectroscopy and discovered a donor defect energy level just below the conduction band and two other semi deep trap levels (Fig. 5a). In Table 3, we have listed few of the DLTS measurement studies alongside the commonly observed defect location with the trap density observed in various 3D halide perovskites. Understanding and reduction of these detrimental trap levels are highly important for the V_{OC} and J_{SC} enhancement of the perovskite solar cell.

Heish et al. [54] studied the impact of intermolecular and interfacial defect density of the perovskite device by considering the three different hole transport layer (HTL) such as P3HT, PBTTTV-h and spiro-OMeTAD. Authors have observed lower defect density in PBTTTV-h and spiro-OMeTAD based device because of the better band edge alignment at the PBTTTV-h/perovskite and spiro-OMeTAD/perovskite interface compared to P3HT/perovskite interface. Xue et al. [55] also studied charge-based DLTS spectroscopy (Q-DLTS) on MAPbI$_3$-based solar cell. Q-DLTS signal was observed to be strongly polarity dependent indicating majority of the defects were present near the perovskite and charge transfer layer interface only.

Table 3 Literature review of defect parameters such as location of defect level energy (eV), type of defects and defect density/cm^3 of various perovskite-based semiconductor measured using DLTS and TAS spectroscopy. Location of defect energy levels and defect density is highly correlated with the device fabrication conditions so these parameter values are only indicative in nature

Perovskite material	Defect level location (eV)/type	Defect density/cm^3	Reference
MAPbI$_3$	One step 0.62, 0.75 Two steps 0.62, 0.76	1.3×10^{15}, 3.9×10^{14} 5×10^{14}, 9.5×10^{14}	[52]
Cs$_x$(MA$_{0.17}$FA$_{0.83}$)$_{(1-x)}$ Pb(I$_{0.83}$Br$_{0.17}$)$_3$	0.57 (hole), 0.74 (electron) 0.2 (donor)	Donor level $= 10^{18}$ Hole $= 0.12\times10^{14}$ Electron $= 2\times10^{14}$	[53]
MAPbI$_3$	0.324 0.46	$\sim10^{17}$	[58]
MAPbBr$_3$ single crystal	0.17 0.20	$\sim10^{8}$ $\sim10^{9}$	[59]
FAPbI$_3$ (mixed with MAPbBr$_3$)	0.46 0.72 0.86	-	[60]
MAPbI$_3$	0.16 (acceptor)	10^{16}	[61]
MAPbI$_3$	0.12, 0.52, 1.42		[62]
MAPbI$_2$Br	0.45, 1.03	$\sim10^{16}$–10^{17}	
MAPbI$_2$Cl	1.25, 0.07		
MAPbI$_3$	0.22, 0.32, 0.40, 0.49, 0.51	10^{17}	[55]
MAPBI$_3$	$\delta = 0.19$ $\beta = 0.37$ $\gamma = 0.37$	$\sim10^{13}$–10^{14}	[51]

Authors have discovered a distribution of defect energy level E_T centered around 0.45 eV having the highest trap density. Reichert et al. [51] studied temperature dependence of DLTS signal on MAPbI$_3$-based solar cell. They characterized the ionic defect distribution in archetypal perovskite (Fig. 5b). As predicted from the previous studies and first principle calculation [34], point defect vacancies such as V_I^-, V_{MA}^-, I$_i^-$, MA$_i^+$ (i stands for the interstitial vacancies) are supposed to dominate the ionic migration in perovskite material. Another work by Reichert et al. [56] has studied the ionic defect distribution by gradually varying the stoichiometry of MAPbI$_3$ from the under-stoichiometric condition to the over-stoichiometric condition using the method previously proposed by Futscher et al. [57] The investigation established V_I^- vacancies in lower stoichiometry, and interstitial vacancies such as I$_i^-$, MA$_i^+$ for over-stoichiometry films were dominating the ionic migration in MAPbI$_3$ perovskite.

3.4 Thermal admittance spectroscopy (TAS)

TAS is yet another powerful technique for the determination of defect type, capture cross section and defect concentration [63]. TAS measures the admittance AS (f, T) of the p–n junction with respect to the simultaneous variation in frequency as well as change in the temperature of the device. The admittance of p–n junction is defined as described below in Eq. 3.12. [42]

$$Y(\omega, T) = G(\omega, T) + i\omega C(\omega, T) \tag{3.12}$$

Table 4 Values of radiative rate constants and charge carrier mobility in different perovskite-based semiconductors where $K_1 =$ monomolecular recombination rate constant (s^{-1}), $K_2 =$ bimolecular recombination rate constant (cm^3-s^{-1}), $K_3 =$ Auger recombination rate constant (cm^6-s^{-1}) and $\mu =$ charge carrier mobility value respectively. Ref. $=$ Reference

Material Perovskite thin films	K_1 (s)$^{-1}$ Ref	K_2 (cm^3-s^{-1}) Ref	K_3(cm^6-s^{-1}) Ref	$\mu = \mu_e + \mu_h$ (cm^2/v-s) Ref
MAPbI$_3$	1.5×10^7 [113] 1.8×10^7 [73] 7.27×10^7 [114]	9.4×10^{-10} [113] 1.7×10^{-10} [73] 15×10^{-10} [114]	3.7×10^{-29} [113] 13.5×10^{-28} [114]	8.1 [113] 35 [115]
MAPbBr$_3$	2.72×10^7 [114]	4.9×10^{-10} [114]	3.4×10^{-28} [114]	17.6 [116]
MAPbI$_{3-x}$Cl$_x$	0.4×10^7 [113] 1.2×10^7 [117]	8.7×10^{-11} [113] $1,1\times10^{-10}$ [117]	9.9×10^{-29} [113] 2.3×10^{-29} [117]	11.6 [118] 33 [117] 40 [74] 27 [97]
FAPbBr$_3$	21×10^6 [117]	11×10^{-10} [117]	1.5×10^{-28} [117]	14 [117]
FAPbI$_3$	7×10^6 [117]	1.1×10^{-10} [117]	0.2×10^{-28} [117]	27 [117]
MASnI$_3$	8×10^9 [119]	1.4×10^{-10} [119]		1.6 [119]
FA$_x$Cs$_{1-x}$PbI$_3$		1×10^{-10} [21]	2.1×10^{-27} [21]	20 [120]
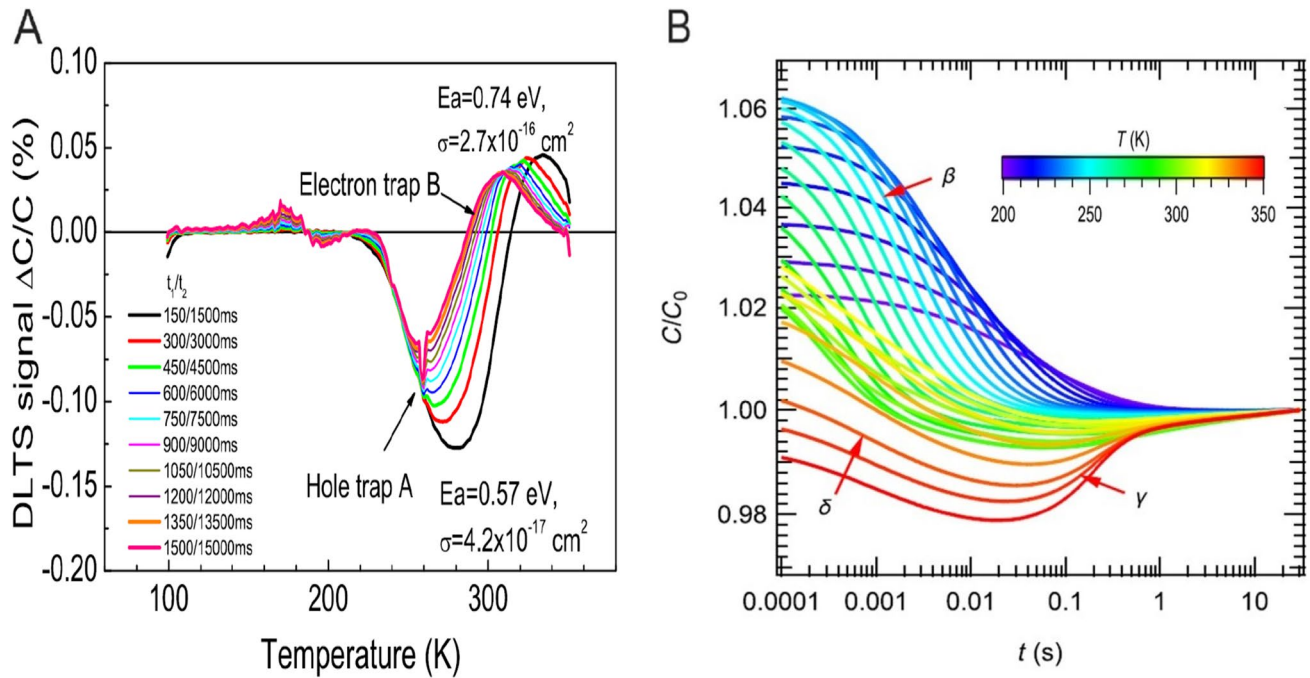
Fig. 5 (a) DLTS spectrum of multi-cation perovskite-based solar cell at various rate windows. The negative peak in the spectrum corresponds to the hole capture defect level, and the positive peak corresponds to the electron capture defect level [53], (b) determination of defect migration in archetypal MAPbI$_3$ perovskite using DLTS measurement. The δ peak was assigned to iodine migration to interstitial site, the β peak was assigned to the MA vacant site, while the γ peak was assigned to the presence of MA$^+$ at the interstitial site. [51]

where ω is the probe frequency, G is the conductance and C is the capacitance of p–n junction. The conductance of the p–n junction is defined by using Eq. 3.13. [63]

$$\frac{G}{\omega} = \Delta C \left(\frac{\omega \tau}{1 + \omega^2 \tau^2} \right) \tag{3.13}$$

Since non-radiative recombination is a thermally activated process, the temperature dependence of emission rate due to the traps is given by Eq. 3.14. [51]

$$e_t = \frac{e^2 N_{eff} D_0}{KT \varepsilon_o \varepsilon_r} exp\left(-\frac{E_A}{KT} \right) \tag{3.14}$$

where N_{eff} is the effective doping density, D_0 and E_A are the diffusion coefficient and the activation energy of the trap states respectively. Emission rate is determined by the gap window rate as described in Eq. 3.11. The characteristic frequency of charge carrier response is related to the dielectric relaxation time of the semiconductor, and it is given by Eq. 3.15. [42]

$$\omega_d = \frac{2\pi}{\tau_d} = \frac{\sigma}{\varepsilon} \tag{3.15}$$

For the input frequencies higher than the characteristic carrier frequency ω_d, free charge carriers are frozen out inside the semiconductor, and it behaves like a dielectric material. [42] Capacitance of a p–n junction under freezeout condition is given by Eq. 3.16 [42] and also known as geometric capacitance of the diode.

$$C = \frac{\varepsilon \varepsilon_0}{d} \tag{3.16}$$

where d is the distance between two electrodes of the device. In order to activate response from the deep lying states, one has to increase the temperature of the device or tune frequency of the input signal in the frequency range comparable to emission rate of charge carrier from the trap states. At much higher frequency $\omega >> e_n$, e_p transport in semiconductor is limited only by the free charge carrier-based mobility so TAS can also be used to measure charge carrier mobilities as well. [64, 65]

Case studies TAS study performed on multi-cation based perovskite by Polyakov et al. is shown below in Fig. 6a, b. [53] They observed a strong freezeout capacitance region and a peak in capacitance below the temperature 250 K as shown in Fig. 6a. They also observed a capacitance and conductance peak shift with increase in the probe frequency. The abrupt increase in the capacitance above temperature 250 K was observed due to the presence of parasitic capacitance of the device. This study also indicates that above 250 K defects does not contribute towards change in the

Fig. 6 **(a)** Measurement of capacitance versus change in temperature at various frequencies using the thermal admittance spectroscopy. **(b)** Measurement of AC conductance versus temperature at different frequencies using thermal admittance spectroscopy for the multi cation based $Cs_x(MA_{0.17}FA_{0.83})_{(1-x)}$ $Pb(I_{0.83}Br_{0.17})_3$ perovskite solar cell. [53]
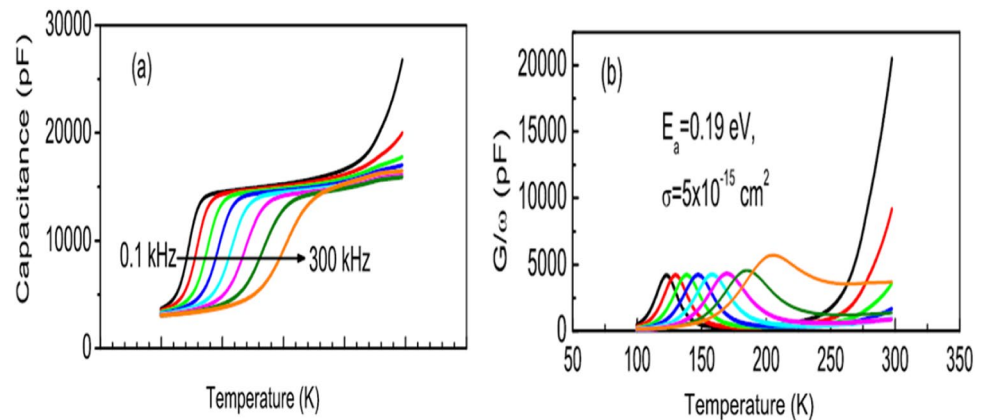
TAS signal. One of the important applications of TAS is the measurement of trap density of states (tDOS) [66], and it is given by Eq. 3.17. [67]

$$N_T(E_\omega) = -\frac{V_{bi}}{qW}\frac{dC}{d\omega}\frac{\omega}{KT} \tag{3.17}$$

Xiao et al. [66] used this relation to calculate tDOS for MAPbI$_3$-based solar cell for two different cases, thermal annealed sample and DMF solvent (vapor) annealed perovskite film. The tDOS for thermal annealed device was found to be 1.8×10^{16}/cm^3, and tDOS for the solvent annealed device was found to be 5.3×10^{16}/cm^3. The tDOS for the solvent annealed device was observed to be 16 times smaller than the thermal annealed device. Hence, solvent annealed device was observed to be better performing than the thermal annealed device; hence, tDOS measurement can also be taken as a direct indicator for better performing device. Wu et al. [68] distinguished surface and bulk defect in the 5 different device of stacks FTO/TiO$_2$/perovskite/Spiro-OMeTAD-Au(device1), FTO/TiO$_2$/PCBA(monolayer)/perovskite/SpiroOMeTAD/Au(device2), FTO/perovskite/Spiro-Au (device3), FTO/TiO$_2$/perovskite/Au (device 4), FTO/TiO$_2$/PCBA/perovskite/Au (device 5). Through TAS measurement, authors have calculated the bulk as well as surface defect density by using the relation $C = qAN_{SS}$ where N_{SS} is the surface defect density states of the perovskite/contact interface. All the different devices showed similar bulk capacitance response indicating same bulk defect density in the range of 10^{17}/cm^3 to 10^{18}/cm^3. This implies that different interface configuration as in different devices from 1 to 5 does not influence the bulk defect density of the perovskite layer. But the calculated interface defect density was found to be different for each case, and the interface defect density was observed to be increasing with the removal of ETL and HTL layers. Authors have attributed change in different device PCE and device degradation

to change in the interface defect density. Awni et al. [69] argued that high-frequency capacitance response of charge carrier in perovskite-based solar cell is due to the charge carrier response of the charges present inside the HTL material. Hence, high-frequency capacitance measurement cannot be taken as a reliable measurement technique for defect distribution in perovskite. Though high-frequency response of perovskite solar cell without HTM layer can be used to calculate bulk perovskite defect properties. However, low-frequency response of the charge carriers can still be used as a reliable method for measurement of defect activation energy. Cho et al. [70] also highlighted the importance of perovskite/charge transfer layer interface. Author has studied Cs-doped thin film under PbI$_2$-rich and PbI$_2$-deficient condition by varying the PbI$_2$ molar concentration in device stack ITO/SnO$_2$/(FA$_{0.9}$MA$_{0.1}$)Pb(I$_x$Br$_{1-x}$)/Spiro-OMeTAD. Through tDOS and photo-aging measurements, Pb-rich device was observed to be prone to the formation of deep level defects and irreversible degradation. Authors have assigned this irreversible degradation to Pb-I antisite formation and un-coordinated Pb creating deep donor like defect levels. Balance stoichiometric and Pb-deficient device was observed to be more stable due to surface passivation of Pb-I antisite defects.

3.5 Radiative recombination and photoluminescence (PL) spectroscopy

Photoluminescence signal is generated due to radiative recombination of photogenerated *e–h*, and emitted photons are detected outside to construct a photoluminescent signal. The spontaneous rate of emission at thermal equilibrium is given by Eq. 3.18. [12]

$$R^0{}_{SP} = \frac{8\pi n_r{}^2}{h^3 c^2}\frac{\alpha(E)E^2}{exp(E/KT) - 1} \tag{3.18}$$

Using Eq. 3.18, the rate of spontaneous emission after an excitation source is given by Eq. 3.19. [12]

$$R_{SP} = R_{SP}{}^0 \frac{np}{n_0 p_0} - R_{SP}{}^0 = K_2 n_i{}^2 \left(exp\left(\frac{\Delta\mu}{KT} \right) - 1 \right) \quad (3.19)$$

The photoluminescence yield generated due to emission of photons is given by Eq. 3.20. [12]

$$Y_{PL}(E) = \frac{1}{4\pi^2 h^3 C^2} \frac{\alpha(E)E^2}{exp\left(\frac{E-\Delta\mu}{KT} \right) - 1} \quad (3.20)$$

Finally, the photoluminescence efficiency is given by Eq. 3.21 [20], and it is the ratio of radiative recombination divided by the total recombination rate happening inside the semiconductor material.

$$\phi(n)_{PL} = \frac{nK_2}{K_1 + nK_2 + n^2 K_3} \quad (3.21)$$

Photoluminescence yield in perovskite semiconductor is found to be increasing with an increase in the excitation intensity which is a great signature of perovskite being a direct bandgap semiconductor. [71, 72] Further, large PL intensity due to the radiative recombination in perovskite also suggests transport in perovskite is dominated by the free charge carrier rather than the exitonic charge transport. Yamada et al. [73] studied the photoluminescence spectrum in MAPbI$_3$ thin film deposited on mesoporous TiO$_2$ by varying the different excitation fluence as shown below in Fig. 7.

At lower excitation intensity, the PL showed a monoexponential decay because at the lower excitation levels only the non-radiative recombination channel is activated. The PL decay time in such case is the non-radiative lifetime of the semiconducting material. At higher excitation intensity, monoexponential decay changes into faster non-exponential decay because of the activation of bimolecular and Auger recombination processes respectively. By observing Fig. 7b, charge carrier lifetime measured from the PL spectroscopy initially stays constant upon changing the excitation intensity and after a certain excitation limits a nonlinear dependence of charge carrier lifetime due to the presence of higher order recombination can be observed. Also, the PL intensity is observed to be increasing linearly, and after a certain limit the quadratic dependence is observed due to the bimolecular recombination processes present in the perovskite semiconductor. The effective PL lifetime at large photon excitation intensity is given by Eq. 3.22. [73] Fig. 8a depicts the observed behavior of different charge carrier lifetime measured using the PL spectrum as a function excess charge carrier density.

$$\tau_{tot|PL} = \frac{1}{K_1 + K_2 n + K_3 n^2} \quad (3.22)$$

Case studies Barugkin et al. [72] studied the temperature dependence of radiative recombination of MAPbI$_3$ thin film using the PL spectroscopy. The PL peak was observed to be red shifting with a decrease in the temperature. Authors described this behavior to the localization of charge carriers near the conduction and valence band edge due to the decrease in the temperature. The K_2 was also observed to increase with the decrease in temperature which is a characteristic feature of a direct bandgap semiconductor. Light absorption coefficient of direct bandgap semiconductor is observed to first increase with increasing in the incident photon energy and become constant towards the high energy wing of the solar spectrum. For the low energy wing,

Fig. 7 (**a**) Photoluminescence measurement of MAPbI$_3$ perovskite at different photoexcitation intensities, at higher intensity photo decay is much faster compared to lower intensities. (**b**) Variation of photoluminescence intensity with the photoexcitation intensity. The rate of charge carrier decay is linear in the low fluence regime (~non-radiative recombination regime) quadratic in the mid fluence regime (~radiative recombination regime) and charge carrier lifetime versus the variation in the excitation intensity of the source determined from the PL decay profile [73]
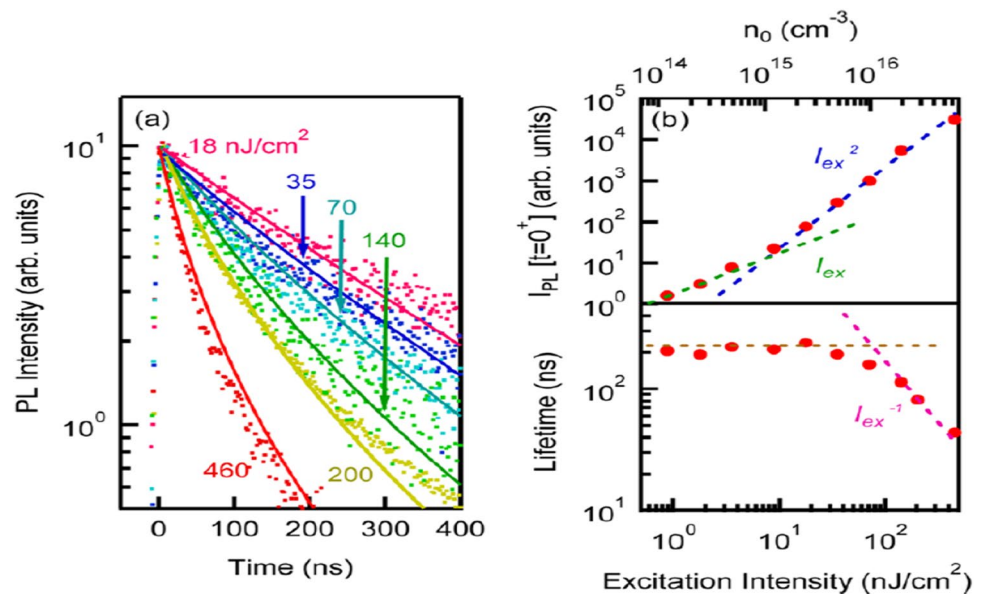
Fig. 8 (a) Variation in the charge carriers lifetime of different recombination processes as of function of excess charge carrier concentration. **(b)** Increase in the internal quantum luminescence efficiency due to photo recycling effect as discussed in Sect. 4 of the review [74]
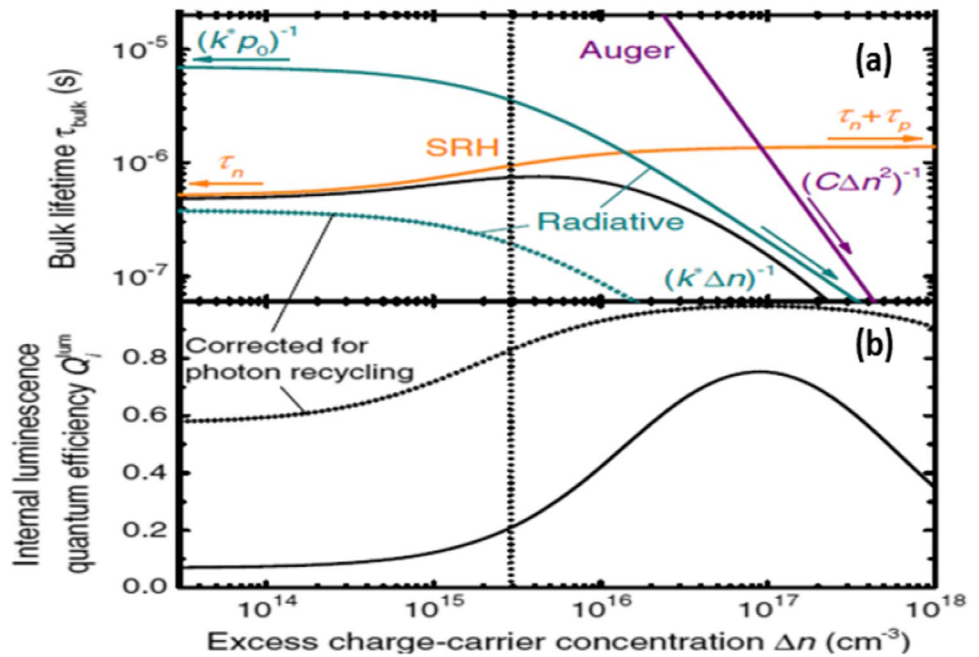
absorption of a semiconductor can be defined by the relation $A = \alpha(E)d$, and the PL yield is observed to increase monotonically with increase in the photon energy (Fig. 9). At the high energy wing of the PL spectrum, by assuming $\alpha = 1$, i.e. a uniform absorption of all photon with different energy and exploiting this behavior of light absorption coefficient of semiconductor into Eq. 3.20 and by rearranging it as Eq. 3.23. [12]

$$ln\left(\frac{Y_{PL}(E)}{10^{23}E^2/cm^2eV-s}\right) = -\left(\frac{E-\Delta\mu}{KT}\right) \qquad (3.23)$$

By plotting Eq. 3.23 and estimating the slope at high energy wing of PL spectrum, the operating temperature of device can be easily determined and the intercept on Y axis at $E = 0$ will yield the quasi-Fermi level separation of the solar cell [74, 75]. For high photon energy wing, the photoluminescence yield scales as $Y_{PL}(E) \propto E^2 exp(-E/KT)$. This situation to estimate the quasi-Fermi level separation and device operating temperature using Y_{PL} is shown below Fig. 9.

Large PL yield is also a quality indicator for a solar cell for obtaining a large V_{OC}. [76] Using the inverse optical reciprocity relation, light absorption coefficient can also be

Fig. 9 Determination of quasi Fermi level separation and device operating temperature containing the perovskite absorber using the photoluminescence experiment in the high energy wing of the photon spectrum where light absorption coefficient remains constant [74]
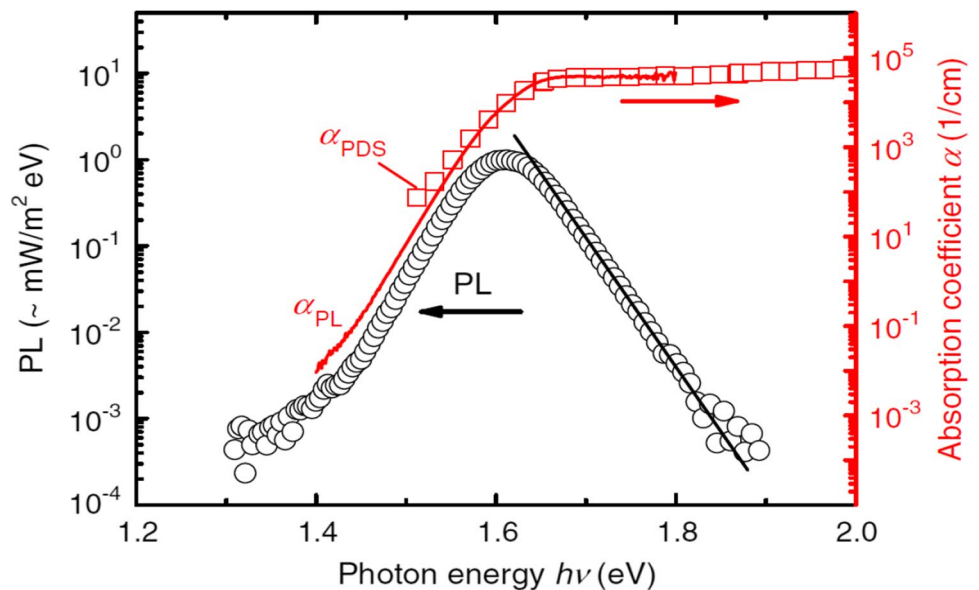
constructed using the PL spectrum. [72] Low temperature PL measurement is also performed to explore the excitonic features in the perovskite material. [77]

3.6 Radiative recombination and electroluminescence (EL) spectroscopy

Electroluminescence spectroscopy is the inverse of photovoltaics process; it is the emission of light due to radiative recombination promoted due to the application of external voltage. The electroluminescence efficiency of solar cell is the ratio of radiative current to the total injected current inside the device and given by Eq. 3.24. [74, 78]

$$(EQE)_{EL} = \tau_{eff}/\tau_R = \frac{\left(K_1 n + K_2 n^2 + K_3 n^3\right)}{\left(K_2 n^2\right)} \text{ or}, (EQE)_{EL} = \frac{J_{rad}}{J_{inj}}$$

(3.24)

Under the radiative limit of the solar cell, $(EQE)_{EL}$ must be equal to unity. The non-radiative V_{OC} is given by Eq. 3.25. [79]

$$V_{OC} = V_{OC}{}^{rad} + \frac{KT}{q} ln(EQE)_{EL}$$

(3.25)

A reduction in the $(EQE)_{EL}$ by a factor of 10 due to non-radiative recombination will reduce the V_{OC} by a magnitude of 60 mV. Okano et al. [80] studied the degradation mechanism of MAPbI$_3$-based solar cell by means of EL and PL imaging techniques. Though spatial distribution of EL was observed identical before and after the device degradation, but the decrease in the EL intensity with time and its temporal evolution was assigned to degradation of the perovskite layer. The photoluminescence efficiency ($\phi(n)_{PL}$) discussed earlier is the indicator for determining the departure of the V_{OC} of a solar cell from its radiative limit. A 100% photoluminescence efficiency indicates $V_{OC} = (V_{OC})_{Rad}$ which is also the maximum voltage that can be extracted from a solar cell. High quality ionic crystalline materials such as GaAs-based solar cell are proven to have as high as 99.7% photoluminescence efficiency [81],while commercialized silicon-based solar cells have photoluminescence efficiency up to 20% even in state-of-the-art based devices. [82] This indicates that, it is difficult to obtain high V_{OC} from the silicon-based solar cell (close its radiative limit of the open circuit voltage).

In case of perovskite-based solar cells, through surface passivation effect, Braly et al. [83] managed to obtain a very high photoluminescence efficiency ~ 92%. By introducing the n-trioctylphosphine oxide (TOPO) on the surface of MAPbI$_3$ perovskite, authors have managed to obtain a V_{OC} of 1.28 V which is 97.1% of the radiative limit of MAPbI$_3$-based absorber. Hameiri et al. [84] studied fast

camera-based PL and EL imaging on perovskite-based solar cell. Further, the correlation between the intensity of luminescence signal and V_{OC} of the solar cell has been explored via understanding the exponential relationship between quasi-Fermi level separation of the absorber layer with the photoluminescence intensity to determine V_{OC} of the solar cell. [85] Time resolved photoluminescence (TRPL) spectroscopy is a widely used technique [4, 86–88] to determine the efficient charge extraction at the ETL/perovskite and HTL/perovskite interface. The rapid quenching of PL signal away from open circuit voltage condition of the solar cell is regarded as a quality measure of the efficient charge carrier extraction at the charge selective and absorber layer interfaces. [89] Baloch et al. [16] studied the photocarrier dynamics at the HTL/perovskite interface by using the TRPL and also performed sensitivity analysis of various parameters such as surface recombination velocity (S_L), interface recombination velocity (S_R), charge carrier mobility (μ) and doping density (N_D) by modeling the PL decay profiles. Usually, the PL signal is measured at the open circuit voltage condition of the solar cell since the radiative recombination at V_{OC} condition is the maximum. But Stolterfoht et al. [90] also measured PL signal as a function of voltage denoted by the symbol PL(V) on the perovskite-based solar cell by varying the HTL thickness and doping concentration. The PL(V) signal was observed to mirror the JV response of the solar cell in the power generating regime, and this also highlighted the correlation between the losses related to the non-radiative recombination process and radiative recombination process. High fill factor (FF)-based devices showed a rapid quenching of PL(V) while moving away from the open circuit voltage to the maximum power point condition of the solar cell. Authors have concluded that PL signal has to be maximized at open circuit voltage condition for obtaining the high efficiency solar cell. Rai et al. [91] studied the effect of perovskite absorber layer thickness on the $(EQE)_{EL}$. Thin perovskite layer was observed to show high $(EQE)_{EL}$ in comparison to the thick perovskite layer because of requirement of the small injection current for the thinner samples. Perovskite-based semiconductors have also found widespread application in light emitting diodes (LEDs), and various researchers have studied the radiative recombination mechanism in perovskite for LED application by the means of EL and PL spectroscopy techniques. [92–95] Kirchartz et al. [96] also prepared a detailed study on the fundamentals of radiative recombination and its relation with EL and PL spectroscopy techniques.

3.7 Charge carrier mobility and diffusion length

The dc conductivity of a semiconductor is given by the relation $\sigma = ne\mu$ where μ is the mobility of free charge carriers. It has been observed that the mobility in typical

cubic perovskite varies as $T^{-1.5}$ where T is the temperature of the device [97]. This indicated the phonon scattering influence on the mobility of charge carriers. [98] Perovskite thin films are highly defect tolerance despite having the presence of a large number of point defects (10^{17}/cm^3). The reason behind this is the large formation energy of deep level states which can directly impact the mobility of charge carriers as discussed earlier. Charge carrier diffusion length can be calculated using the relation $L_D = \sqrt{D\tau}$, D is the diffusion coefficient of charge carrier and related to the mobility by the Einstein relation as shown below in Eq. 3.26. [37]

$$D = \frac{\mu KT}{q} \qquad (3.26)$$

Diffusion length is the maximum length of charge carriers which they can travel before recombining inside the material. Mobility in disordered semiconductor (organic semiconductor, a-Si) follows Langevin limit of the recombination. [99] In Langevin limit by assuming a hole in the semiconductor material forms a Coulomb potential well around an electron, and the probability of recombining e–h radiatively is decided by equilibrium between thermal energy and the potential energy of hole and electron charge assembly as described below in Eq. 3.27. [20]

$$KT = \frac{q^2}{4\pi\varepsilon_r\varepsilon_0 r} \qquad (3.27)$$

Since the potential energy of the charge carrier is the derivative of electric field (E) and by using the Ohms law relation $J=qn\mu E$, the Langevin limit of recombination is given by Eq. 3.28. [99]

$$\frac{K_2}{\mu} = \frac{q}{\varepsilon_r\varepsilon_0} \qquad (3.28)$$

Perovskite-based semiconductors are observed to defy the Langevin limit (Eq. 3.28) by 4 to 5 orders of the magnitude; hence, charge carrier mobility in a perovskite semiconductor is limited only due to the phonon-electron scattering [99]. The reason behind this is the defect tolerance nature of perovskite absorbers, and this makes this material highly suitable for the optoelectronic applications. [29] Mobility and the diffusion length in perovskite-based semiconductor can be measured using various characterization techniques. We have listed one of the most prominent experimental techniques to measure charge mobilities using transient terahertz absorption spectroscopy (Fig. 10).

3.8 Terahertz transient absorption spectroscopy

Perovskite photoconductivity is observed to be compatible with Drude response as described by Eq. 3.29. [100]

$$\sigma_d = \frac{\sigma_{dc}}{1 - i\omega\tau} \qquad (3.29)$$

$\sigma_{dc} = \frac{ne^2\tau}{m}$ is the ohmic response of the conductivity. If the scattering rate of charge carriers is comparable to THz frequency, then both the real and imaginary parts of the photoconductivity are observed to be finite, and this can be used for the determination of mobility of free charge carrier by using the Drude response $\mu = \frac{q\tau}{m*}$; $m *$ is the effective mass of the electrons. [100] In terahertz absorption spectroscopy, pump (laser pulse beam as an excitation source) is used to generate free charge carrier and light
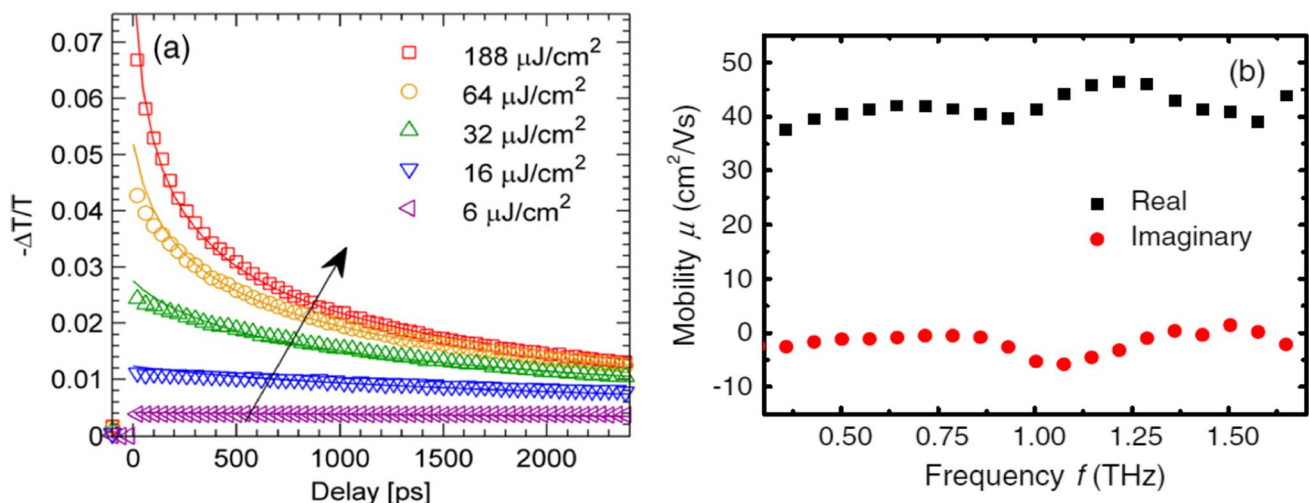
Fig. 10 (a) Measurement of normalized photoconductivity transient versus pump-probe delay time of dual source vapor-deposited MAPbI$_{3-x}$Cl$_x$-based perovskite measured using pump-probe terahertz absorption spectroscopy at various excitation fluences showing domination of various regime of recombination processes by the decay rate of transient signal. [99] **(b)** Determination of total charge carrier mobility $\mu=\mu_e+\mu_h$ using the real part of mobility determined from the transient absorption spectroscopy [74]

is used as a probe signal. Due to pump-induced charges, the change in electric field E is related to change in the photoconductivity of the sample given by Eq. 3.30. [100]

$$\frac{\Delta E}{E} \propto \frac{\Delta \sigma}{\sigma} \tag{3.30}$$

$\frac{\Delta \sigma}{\sigma}$ is known as the normalized photo conductivity, and $\Delta \sigma$ is the transient response of photoconductivity of the semiconducting sample. Transient absorption spectroscopy generates signal as normalized photoconductivity with respect to delay time between pump and probe signals. Delay time between pump and probe signal is chosen such that it matches with the photoexcited relaxation process time. Transient photoconductivity signal at low fluence levels shows decay due to the monomolecular recombination channel as the fluence increases the other recombination channels also begins to respond, and this situation is shown in Fig. 10a.

Case studies In some of the early studies, Wang et al. [101] investigated the time resolved transient spectroscopy of MAPbI$_3$ in under-stoichiometric and over-stochiometric condition of PbI$_2$. Perovskite film with deficient PbI$_2$ concentration showed a faster relaxation time than the perovskite with excess PbI$_2$ concentration. Authors have attributed this slow dynamic to the surface passivation impact of excess PbI$_2$. Figure 10a is the photoconductivity spectrum of mixed halide MAPbI$_{3-x}$Cl$_x$-based perovskite, and this spectrum can be used to extract the real and imaginary parts of the charge carrier mobility using the Drude model of electrical conduction. The real part of mobility which is the sum of electron mobility (μ_e) and hole mobility (μ_h) stays constant as shown in Fig. 10b. By assuming the equal mobilities for electrons and holes, the observed mobility values for electrons and holes were 20 cm^2/V-s (Table 4).

4 Factors affecting recombination coefficients and their magnitude in perovskite

4.1 Photon recycling (PR)

Photon recycling (PR) is the repeated reabsorption of the spontaneously emitted photon due to radiative recombination. PR effect is observed to cause a reduction in the rate constant K_2 because of large relative refractive index of perovskite-based semiconductors ($n_r = 2$–2.6), [102] and radiatively emitted photons are observed to have low escape probability out of the device. [18]

Shockley and Queisser did not consider the impact of PR on the calculation of ultimate PCE limit for single

junction solar cells. PR is observed to enhance the overall photoluminescence yield and hence imparted to improve the V$_{OC}$ of the solar cells significantly. [103] Total radiative current detected externally is given by Eq. 4.1. [18]

$$J_0{}^{rad,ext} = q \int_0^\infty \alpha(E)\phi_{bb}(E)dE \tag{4.1}$$

The relationship between radiative current generated internally and detected externally is given by Eq. 4.2. [18]

$$J_0{}^{rad,ext} = p_r J_0{}^{rad,int} \tag{4.2}$$

p_r is known as the probability of recapturing the photon inside the semiconductor. The total internal radiative current generated due to the impact of PR is given by Eq. 4.3. [18]

$$J_0{}^{rad,int} = q \int_0^\infty 4\alpha(E)n_r{}^2 d\phi_{bb}(E)dE \tag{4.3}$$

The impact of PR on enhancement on the open circuit voltage of the solar is given by Eq. 4.4. [18]

$$\Delta V_{OC}{}^{PR} = \frac{KT}{q}ln\left(\frac{J_0{}^{rad,int}}{J_0{}^{rad,ext}}\right) = \left|\frac{KT}{q}ln(p_r)\right| \tag{4.4}$$

Through repeated absorption, bimolecular recombination constant also decreases by a factor as shown below in Eq. 4.5. [104]

$$K_2 = \frac{K_2{}^*}{1 - p_r} \tag{4.5}$$

where K_2 is the modified radiative recombination constant (detected externally) due to the impact of PR inside the semiconductor material.

4.2 Rashba effect

Another effect that influences the rate of radiative recombination process in perovskite semiconductors is the Rashba effect. Magnetic field produced due to the spin orbit coupling in perovskite material splits the conduction and valance band edge in the k space. [105] The spin degenerated band edges will assign an overall indirect like bandgap characteristic to perovskite semiconductors. [106] Due to this indirect nature of the perovskite bandgap, the radiative recombination rate constant K_2 is also observed to slow down. Radiative recombination is observed to be reducing due to the presence of spin–orbit forbidden transition between the photogenerated charge carriers. [105]

4.3 Polaron formation

Inside a highly polarizable lattice such as metal halide perovskites, atoms fluctuate more about their mean position; due to these atomic displacements, there exists a coupling between phonon produced due to the atomic displacement and charge carrier induced by the light absorption. Such Coulombic coupling interaction between polarons and free charge carrier forces electrons to be trapped inside a potential well created due to the atomic displacement of ions about their mean position. Polarizability of the medium is defined by reciprocal of the relative dielectric constant $\varepsilon(\infty)$ measured at the high-frequency regime of dielectric relaxation. Perovskite is observed as a highly polarizable semiconductor because of the small value of relative dielectric constant $\varepsilon(\infty) = 5$. [15] Based on the interaction between phonon and electrons, polarons are divided into two categories, long range polarons and small range polarons. [15] Large polarons exist over multiple lattice sites, while small polarons exist in a very short range only. [107] Small polaron formation in perovskite is also identified to be a probable reason for reversible photodegradation. [108] Further compositional engineering such as mixed cation perovskites are also observed to enhance the stability of the metal halide perovskite by the formation of small polarons. [109, 110] The binding energy of the large polarons is given by Eq. 4.6 [15] where R_P is known as the polaron radius.

$$E_p = -\frac{e^2}{4}\left(\frac{1}{\varepsilon\infty} - \frac{1}{\varepsilon_0}\right)\frac{1}{R_P} \qquad (4.6)$$

The coupling strength for large polaron distributed over multiple lattice sites is given by Eq. 4.7. [111]

$$\alpha_F = \frac{e^2}{h}\left(\frac{1}{\varepsilon_\infty} - \frac{1}{\varepsilon_0}\right)\sqrt{\frac{m}{2h\omega}} \qquad (4.7)$$

$\varepsilon(\infty)$ and $\varepsilon(0)$ are the high and low-frequency dielectric constants of the semiconductor, and ω, m are the phonon frequency and effective mass of the electron respectively. Polarons are charged quasi particles; hence, a short-range repulsion between oppositely charged polarons always prevails. Polarons screen carrier-carrier scattering and carrier-defect scattering and hence assist in reducing the rate of the bimolecular recombination [112]. This short Columbic repulsion is found to be decreasing the radiative recombination rate of the perovskite materials by repelling the photogenerated free charge carriers away from each other. Electrons and phonon in metal halide perovskite interact through two different interactions, i.e. acoustic deformation and Fröhlich interaction. [107] The acoustic deformation arises from the distortion in crystal structure due to the thermal vibrations of atoms, and it induces the interaction between acoustic phonon and electrons of the

semiconducting material. The Fröhlich interaction arises due to local electric field induced by the polarizability of the ionic lattice. As measured from time resolved terahertz spectroscopy, the charge carrier scattering time varies as $\tau \propto T^{-1.5}$ where T the temperature of the device. [97] This kind of temperature dependence of scattering time is only observed when the charge carrier transport is limited by the scattering due to acoustic phonon only. Miyata et al. [112] studied large polaron formation in MAPbI$_3$ and CsPbBr$_3$-based 3D perovskite and concluded that large polaron formation in perovskite is independent of the type of cation used. Large polaron formation was observed due to the deformation of PbX$_3^-$ framework, though polaron formation time was observed to be less in MAPbI$_3$ (0.3 ps) compared to CsPbBr$_3$ (0.7 ps) -based perovskite.

5 Defect passivation in perovskite

The photovoltaic performance of perovskite solar cell (PSC) is highly influenced by the presence of the defects in the perovskite absorber layer. To achieve the high PCE in PSCs, the defect passivation techniques are highly important. Most of the intrinsic point defects in perovskites are observed near to the band edges; however, deep level defects such as the migration of ions, interfacial defects and grain boundaries can gravely impact the stability and optoelectronic properties of perovskites. These defects can be prevented by using the different passivation strategies such as the introduction of cation or anion, [121, 122] additive approach, [123] suppression of ion migration, [124] grain boundary engineering, [125] interfacial engineering, [126] antisolvent method [127] and deposition method, [128] which are briefly discussed in the next section. We have also listed various defect engineering strategies and their outcomes in Table 5 studied on various APbX$_3$-based perovskite materials.

5.1 Defect passivation using stoichiometric/ non-stoichiometric material engineering

The Pb-based vacancies that can form deep level defects originate in the lead halide perovskite due to the excitonic stress [129], incomplete reaction [130], contamination and aging stress. [131] These defects or vacancies act as strong non-radiative recombination centers and hamper the long-term stability of the perovskites. The lead vacancies in MAPbI$_3$ can be prevented by the incorporation of excessive concentration of MAI in the precursor and keeping a deliberate Pb-I$_2$ deficient condition during the formation of precursor. Zhang et al. [132] have reported the passivation of lead vacancies in inorganic perovskite by introducing

Table 5 Various defect engineering strategies employed in $APbX_3$-based perovskite materials

Passivation technique	Passivation agent	Target defect	Mechanism	Perovskite material	PCE (%)	Reference
Material engineering	In situ PbI_2	Halide vacancy	Strain relaxation	$(FAPbI_3)_{1-x}(MAPbBr_3)_x$	19.55	[140]
	I_2/antisolvent washing	Halide vacancy	Filling	$MAPbI_3$	21.33	[220]
Metal cation doping	Na+	MA vacancy	Substitutional filling	$MAPbI_3$	15.14	[221]
	KI	MA and halide vacancy	Filling and immobilizing	$(CsFAMA)_{0.9}K_{0.1}Pb(I_{0.85}Br_{0.15})_3$	21.50	[222]
Zwitterion	QAHs	Ion vacancy	Hydrogen bonding and electrostatic interaction	$FA_{0.85}MA_{0.15}Pb(I_{0.85}Br_{0.15})_3$	21.00	[223]
Lewis acid & Lewis base	IPFB	Under coordinated I^-	Halogen bonding	$MAPbI_xCl_{3-x}$	15.70	[152]
	Pyridine	Under coordinated Pb^{2+}	Coordinate bonding	$MAPbI_3$	18.50	[224]
	DTA	Under coordinated Pb^{2+}	Coordinate bonding	$MAPbI_{3-x}Cl_x$	21.45	[225]
Additives	Zinc porphyrin	Under coordinated Pb^{2+}	Coordinate bonding	Cs, FA, MA perovskite	20.50	[226]
	F4TCNQ	Metallic lead	Coordinate bonding	$MAPbI_3$	16.07	[227]
Interfacial layer passivation	Fullerene derivative	PbI_3^- antisite (at grain boundary)	Coordinate bonding	$MAPbI_3$	17.63	[228]
	PTTA	Ion migration	Grain boundary passivation	$MAPbI_{3-x}Cl_x$	19.04	[126]
	PMMA	I^- vacancy	Coordinate bonding	$Cs_{0.07}Rb_{0.03}FA_{0.765}MA_{0.135}PbI_{2.5}Br_{0.45}$	20.40	[229]
Film passivation	Heat	Halide vacancy, ion migration	Strain relaxation, grain boundary passivation	$MAPbI_3$	15.60	[230]
	VASP	Ion migration	Grain boundary passivation	$FA_{0.81}MA_{0.15}PbI_{2.55}Br_{0.45}$	20.47	[231]

the anionic doping. The defect states were observed to reduce with the introduction of PbI_2-rich and PbI_2-poor precursors. The excess amount of PbI_2 was observed helping in the formation of coordination bond between the two grain boundaries, which leads to the non-stoichiometric compositional growth condition. The PbI_2-rich precursor was observed to reduce the defect density by passivating the local grains. [133, 134] Furthermore, PbI_2-poor precursor has also been observed to reduce the deep level interstitial iodine vacancies in $MAPbI_3$ crystal.

5.2 Defect passivation of metal cations and anions in perovskite semiconductors

The A-site, B-site and X-site defects in ABX_3 perovskite structure can be passivated with the introduction of various selective cations and anions. Because of the cations/anions interaction with the defect site of the ABX_3 by donating/accepting the electrons, defect passivation bonds are observed to form among the selective cations or anions with the defect sites. The cations are observed to passivate the A-site, B-site defects, and anions are observed to

passivate the X-site defects respectively in the ABX_3 perovskite structure. A-site, B-site and X-site defect passivation can be established by incorporating the different metal cations and anionic passivators in the perovskite material. There are several metal cations reported for passivating the negatively charged defects, which are created by the migration of A-site cation, B-site cation and antisite defects in ABX_3 perovskites. These negatively charged defects can be passivated with the introduction of monovalent metal cations such as Na^+, K^+, Rb^+, divalent metal cations Mn^+, Ni^{2+}, Cd^{2+}, Ca^{2+}, Sn^{2+}, and trivalent metal cations Al^{3+}, Eu^{3+}, Bi^{3+}. [135] Since Na^+ ion has the similar atomic radius as the MA^+, so it can be used for the A-site vacancy passivation in the perovskite. Na^+ ion is observed to passivate the grain boundaries by forming the ionic bond with negatively charged defects present at the boundaries and also observed to enhance the grain size of perovskite crystals, which facilitate the formation of pinhole-free perovskite films. [131, 136, 137] Son et al. [121] reported the migration of A^+ site cation is the primary reason for the observed *JV* hysteresis in perovskite-based device, and the hysteresis effect has been suppressed by incorporating the optimum amount of

K^+ ions. The atomic size of K^+ is well suited to occupy the octahedral interstitial sites and prevented the I^- migration by forming the ionic bond with I^-. B-site defects are observed to be passivated by doping the perovskite with the divalent cation and alkaline earth metal cations. [138–140] The divalent metal cations are observed to form coordination bond with the halides present in the perovskite. Doping with Cd^{2+} ion is observed to increase the vacancy formation energy at the B-site by suppressing the ionic migration and creating the lattice strain. To overcome such a high activation energy barrier by the B-site cations is very difficult, which results in the defect passivation of the B-site cation in perovskite. [139] The positively charged defects in halide perovskites are observed due to the lack of coordination between Pb ions, iodine vacancy and antisite defects. The commonly used anionic passivators for defect passivation are F^-, Cl^-, Br^-, I^- and the halogen functional groups. [141] Li et al. [122] used NaF as an anionic passivator for the halide perovskite and observed F^- anion creates hydrogen like bonding with the A-site cation, which provided the important surface stability to the perovskites structure. Tan et al. [142] have reported the X-site defect passivation with Cl^- as an effective passivating agent at the interface by forming Pb-I antisite and Pb-Cl antisite. The defect formation energy of Pb-Cl antisite was observed higher than the Pb-I antisite, which indicates the antisite defects were suppressed with the presence of interfacial Cl atoms. Thus, selective anionic passivators are capable of passivating uncoordinated halides via the hydrogen bonding.

5.3 Grain boundary defect passivation engineering

Defects are usually accumulated at the grain boundaries, and these grain boundary defect are observed to act as strong non-radiative recombination centers. To overcome this problem several additives engineering have been reported by the various researchers such as the introduction of zwitterions, Lewis acids (e.g. fullerene and their derivatives) [143], Lewis bases (O donor, S donor, N donor) for the passivation of grain boundary defect [144], and these grain boundary passivation strategies are discussed below in the next section.

5.3.1 Defect passivation by using the zwitterions

The individual anionic and cationic passivators as discussed in the previous section are only capable of passivating a single kind of point defect at a time, but zwitterions are observed to passivate both the negatively and positively charged point defect simultaneously. The most commonly used zwitterion passivators are mainly metal-based small molecule and organic molecules. Incorporation of ChCl zwitterion to the $MAPbI_3$ perovskite is observed to reduce the MA^+ cation-based defects on the perovskite surface by occupying the octahedral positions, and Cl^- ion is observed to passivate the PbI_3^- antisite defects. [145]

5.3.2 Defect passivation by using the Lewis acid

The uncoordinated I^- and antisite PbI_3^- act as a deep recombination center when present near the surface and grain boundaries of $MAPbI_3$ thin film, and these states can be passivated by using the Lewis acid. Fullerene and their derivatives [143, 146, 147] have proven as the most effective defect passivator because they are observed to have excellent electron-accepting properties and also observed to create the strain inside the perovskite thin film. Shao et al. [143] reported that Lewis acids can make stronger hydrogen like bonding with uncoordinated I^- and antisite PbI_3^- defects. The formation of hydrogen bond increases the charge transfer at the interface, which helps in passivating the defect present at the perovskite surface.

5.3.3 Defect passivation by using the Lewis base

Lewis bases have characteristics of donating a pair of nonbonding electrons; these nonbonding electrons are capable of making bond with uncoordinated Pb^{2+} or Pb clusters present in perovskite and passivate them by forming the adducts. Noel et al. [144] reported Lewis base defect passivation by using the nitrogen and sulphur functionalities molecules having the capability of donating the pair of nonbonding electrons. deQuiletters et al. [148] have investigated trioctylphosphine oxide, octadecanethiol and triphenylphosphine Lewis base for defect passivation in perovskites. Authors have demonstrated the passivation capabilities of Lewis bases and found enhancement in PL lifetime of charge carriers from 0.9 to 8.85 µs. Some other reports also highlighted the importance of reduced graphene oxide, thiophene, pyridine and amine containing compound reported as an effective Lewis base defect passivator. [149–152]

5.3.4 Defect passivation by using the additives

The additives also play a vital role in defect passivation of the perovskite thin films. Tsai et al. [153] incorporated 1,8-diiodooctane (DIO) into the perovskite precursor and observed the uncoordinated Pb ions coordinated with DIO, which passivated the negatively charged defect and enhanced the overall PCE of perovskites. Zhao et al. [154] introduced the excess amount of MACl into perovskite precursor solution; authors have found due to its conformal characteristic, it helps in reducing the undesirable defect branches in perovskite crystals. Hu et al. [155] reported the significant improvement in the stability of perovskite with the addition of rare earth metal, and the device was observed to retain 90% PCE for 1700 h at elevated temperature.

5.4 Interfacial engineering

Since passivating agent is observed to dissolve inside the perovskite precursor solution, there always exists a deviation in the bulk properties compared to the surface properties of perovskite, which leads to the introduction of interface-induced recombination. [156, 157] The interface-induced recombination can be prevented by making use of interfacial engineering. Zhang et al. [158] introduced ultrathin polarized ferroelectric polymer at the perovskite interface and obtained an optimum favorable energy band alignment for high efficiency perovskite-based solar cell. Zhou et al. [159] through controlled formation of the absorber layer and maintaining good carrier extraction at the electrodes by reducing the non-radiative recombination at the interface managed to improve the PCE significantly from 16.6 to 19.3%. Recently, researchers have also reported the mechanism of back transfer recombination process at the interface by using the poly (3-hexylthiophene) as a hole transport layer, which decreases the back transfer recombination process at the HTL/perovskite interface. [160] $PC_{61}BM$ and PMMA explored as a buffer layer between the ETL and perovskite layer are observed to suppress the interfacial recombination centers. [161, 162] The conjugated electrolyte introduced between the PTAA and perovskite is also observed to reduce the detrimental interfacial defect. [163] To enhance the PCE beyond 20% for the *p-i-n* perovskite-based solar cell, Albrecht et al. [164] reported replacement of polymer hole selective layer with the self-assembled monolayer of carbazole-based phosphonic acid. The introduction of LiF between [163, 165] the ETL/perovskite layer was observed to reduce the C_{60}/perovskite interface losses and led to enhancement in the V_{OC} of the solar cell. Jeong et al. [166] reported an effective and simple interface engineering strategy by introducing the cost-effective, stable and dopant-free HTM polymer gallium(III) acetylacetonate into poly(3-hexylthiophene), and devices showed remarkable improvement in the PCE (~24.6%). Recently, several other effective techniques were also reported to passivate the interfacial defects with the application of various interlayers such as polymer, oxides and fullerene derivatives. [161, 167–170]

5.5 Antisolvent vapor-assisted crystallization

Antisolvents cannot dissolve the solute particles but are miscible with the solvent of the solution. In this process, antisolvent interaction with the precursor solution of perovskite makes the overall solution to a supersaturated level, and the supersaturated solution further undergoes coprecipitation process; thus, the high-quality perovskite films are formed. Single-crystal perovskite grown using the antisolvent vapor-assisted crystallization is observed having the superior optoelectronic performance such as mobility, charge carrier diffusion length, charge carrier lifetime compared to microcrystalline perovskite thin films. [171–173] Since growing single crystal on a substrate requires high nucleation formation energy, antisolvent vapor-assisted crystallization is observed to generate an ultrasonic pulse, which results in overcoming the barrier to form a nucleus on the surface of the substrate and provided a defect-free high quality crystalline film of perovskite. [174] The boiling point of solvents (DMF and DMSO) used in the perovskite film synthesis is high, and hence the solvent evaporation rate during spin coating process is low, which hampers the crystallization process and caused the formation of defects in the film. With the addition of non-polar solvents in antisolvent dripping, the solubility of perovskite in solution is reduced, and hence it promotes the effective nucleation and crystallization. [171, 175] Hossein et al. [176] investigated the role of antisolvent optimum temperature for dripping during spin coating process to achieve the best quality films. Wen et al. [177] reported controlled supersaturation and nucleation rate with the mixed antisolvent by optimizing the different antisolvent ratio, which contributed towards growth of large crystalline grain boundaries. The thermodynamics of nucleation process for the various antisolvents have been reported by Liu et al. [178] which provided the crystallization kinetics of perovskite thin film by incorporating the various antisolvents. Tidhar et al. [127] reported the passivation of defect using the antisolvent vapor-assisted crystallization method by alcohol-based antisolvents for $MAPbBr_3$ perovskite. Shi et al. [179] replaced the alcohol-based antisolvent with the dichloromethane (DCM) and produced a defect-free $MAPbI_3$-based single crystal material. Green antisolvents such as petroleum ether, ethyl acetate and iso propanol, ethers diethyl ether, anisole, diisopropyl ether (DIE) are also employed during the fabrication of perovskite-based solar cells. [180–183]

5.6 Optimization of thin film formation

Various processing techniques provide unique perovskite film properties based on the phase formation and the formation of the defect states. [128, 184–186] The kinetics and thermodynamics parameters of these techniques are governed by tuning the annealing temperature, ramping rate, time and introduction of various solvents. [187] Vacuum deposition technique has poor control on the temperature of reactant species and substrate, which leads to nonideal stoichiometry in the thin films of the perovskite. Several concepts are reported regarding improving the morphology of the thin film formation and to minimize the defect density in the perovskite films. These are the incorporation of mesoporous particles and different phase formation with the optimized annealing process. [188–190] Xiao et al. [191]

studied the inter-diffusion of perovskite precursor to tune the composition of the perovskite films.

5.7 Other recent defect passivation strategies

Several recent defect passivation strategies have been reported by various research groups as the surface passivation of the perovskite layer, conversion of extended imperfection to wide bandgap and surface passivation of the carrier transport layer. [192–194] Surface passivation techniques to reduce the detrimental surface defect and dangling bonds have widespread application even in the state-of-the-art commercialized silicon [195–197] as well as GaAs [198, 199] -based solar cells. Surface states and dangling bonds cause deep level defects in bandgap of the semiconductor materials. The contribution of the surface states to the non-radiative recombination process is mainly accessed by the surface recombination velocity. In principle, an ideal surface having zero recombination due to the absence of surface states has zero surface recombination velocity. While extremely bad surfaces having infinite recombination centers have infinite surface recombination velocity. Surface passivation techniques to mitigate defects at the surface have also started to gain attraction in perovskite-based solar cells. He et al. [200] used triphenyl(9-ethyl-9H-carbazol-3-yl)-phosphonium bromide (TCPBr) and iodide (TCPI), as a surface passivator in between the HTL and perovskite interface. Authors have confirmed the effectiveness of surface passivation by measuring the charge carrier dynamics at the HTL/perovskite interface by using the TRPL spectroscopic technique. The increase in PCE and reduction in the hysteresis behavior of the fabricated solar cell were assigned to the effect of surface passivation of the perovskite layer. Further, the hydrophobic nature of the passivating agents was also observed to reduce the moisture penetration and prompted the device stability. Cao et al. [201] modifies the poor chemical compatibility of ZnO ETL layer with the perovskite absorber by passivating the ZnO surface using the thin layer of MgO and protonated ethanolamine (EA). Because of the surface passivation effect, perovskite solar cell with high PCE and hysteresis free device was obtained. The device was observed to be air stable for 300 h when encapsulated by the graphene layer. Jokar et al. [202] studied the doping effect of bulky organic cations with ethylene diammonium diiodide (EDAI$_2$) and butylammonium iodide (BAI) as additives to passivate the lead free perovskite FASnI$_3$ surface. Addition of BAI additive altered the perovskite crystal orientation growth, while EDI$_2$ facilitates the formation of pinhole free thin film and suppresses the oxidation of Sn^{2+} state to the Sn^{4+} state. Small molecular material such tetratetracontane (TTC,CH$_3$(CH$_2$)$_{42}$CH$_3$) incorporated by Li et al. [203] at the fullerene/perovskite interface assisted in reduction of the electron recombination and enhancement in the PCE of the planer perovskite device. Due to the hydrophobic nature of the small molecular material device, it retained 87% of its PCE in air under the constant exposer. Jiang et al. [194] introduced the organic halide salt phenethylammonium iodide (PEAI) layer at the interface of FA-MA mixed perovskite and HTL. Through TRPL study, authors confirmed the surface passivation impact of the PEAI material by obtaining an efficient photo generated charge carrier extraction. The obtained V_{OC} of the device was matched with 94.4% of its Shockley–Queisser limit. Novel indacenodithieno(3,2-b) thiophene (IDT-ThCz)-based small molecule (SM) as additive developed by Choi et al. [204] facilitates the surface passivation of the perovskite surface. The fabricated device using passivated perovskite surface was observed to retain 95% of its PCE up to 500-h storage at elevated temperature condition (85 °C). The ionic defects at the surface and grain boundaries usually passivated through Lewis acid, Lewis base or through ionic bonding passivation mechanism. However, another way to passivate the surface and grain boundaries defects is by chemically converting the extended imperfections to the wide bandgap materials. [205, 206] The wide bandgap hinders the charge transfer between the perovskite grains and interface by creating the electronic barrier, and when the charge reaches to the wide bandgap wrapping layer, these charges are reflected back into the bulk and thus passivate the grain boundaries and interfacial defects. The choice of charge transport material also plays a crucial role to get high performance of PSCs since at the interface band bending, charge accumulation and dipole generation are widely present. [207] Thus, charge transport layer must be optimized to achieve a favorable energetic alignment and have a good charge transfer interface with the active perovskite layer. Various charge transport layer (CTL) passivation strategies have been also reported such as by using the various additives, PTTA [208], EDTA [209], NH$_4$Cl [210], Cl$_2$ [211]. Abuhelaiqa et al. [211] explored doping of SnO$_2$ charge transport layer with tin-bis-(acetylacetonate) dichloride and tin-bis-(acetylacetonate) dibromide and observed the defect passivation effect of SnO$_2$ layer. Other doping methods to improve the performance of CTL is by the introduction of Cu$^+$/Li$^+$/Mg^{+2} metal cations inside the CTL to enhance the conductivity. [212] Okada et al. [213] deposited the mixed layer of polyvinyl carbazole and PCBM over TiO$_2$ CTL and observed the significant improvement in the PCE. The deposition of dense SnO$_2$ layer at the interface by ALD method is also observed to improve the performance of CTL in perovskite-based solar cells. [214] The practical application of PSCs is limited due to poor stability, and large efforts have been made to enhance the stability of PSCs. Those efforts are through the device encapsulation [215], interface engineering [194], phase stabilization

[216] and grain boundary passivation [217] to achieve the device longevity. The operational stability of PSCs is highly dependent upon migration of charge defects inside the ionic perovskite crystal. These charged defects can be passivated by the introduction of different molecular passivator, but during the high temperature and high humidity condition these secondary bonds formed between passivator molecule and perovskite gets easily broken which reduces the passivation effect. [218] To address this issue, Zhao et al. [219] reported strategically designed passivating agents to investigate the effect of the various functional group and their interaction energies with the perovskite ionic defects, which also provided the correlation between the performance and longevity of the passivation effect.

6 Conclusions

In this review, we have discussed the fundamental physics of defect formation, recombination mechanisms and various characterization techniques to estimate the defects and recombination pathways. Using thermodynamics and first principle calculations, we have summarized the formation energy of the various point defects based on their location in perovskite material energy bandgap. Ionic migration of MA^+, Pb^{2+}, I^- into the vacant sites and on the basis of defect formation energy, MA_I and V_{Pb} defects are observed to be the dominating point defect type in pristine perovskite. Perovskite semiconductor despite having presence of large numbers of point defects displays unique defect tolerance nature where physical properties such as charge carrier mobility and lifetime are observed to be unaltered by the bulk point defects. We have described the role of various defects in the different recombination process, whereas deep level defects impact the photovoltaic performance significantly by acting as strong non-radiative recombination centers in perovskite semiconductor. Bimolecular recombination mechanism in perovskite semiconductor is a complicated phenomenon affected by various other processes such as formation of polarons, Rashba effect and photon recycling. The value of bimolecular recombination rate in perovskite is observed to be very close to high quality crystalline inorganic semiconductor GaAs. [87] By using various spectroscopic characterization techniques such as capacitance, photoluminescence, electroluminescence, transient terahertz spectroscopy, it is possible to analyze the role of defects on the recombination losses in perovskite-based solar cells. Quenching of photoluminescence yield and photoconductivity is utilized to determine the effective bulk lifetime of charge carriers in the perovskite thin films. Using the capacitance spectroscopic measurements, various researchers highlighted the importance of surface and interfacial defects being the most

determinantal for the perovskite devices. Although researchers still need to explore the impact of point defects on the device parameters, also the individual contribution of point defects and interfacial defects still needs to be identified. Other complementary techniques such as space charge limited current (SCLC) method [50, 232–236], electron beam induces current (EBIC) method [237], scanning kelvin probe microscopy [44, 238], X-ray diffraction spectroscopy [239], positron annihilation spectroscopy [240] are also widely explored to determine the impact of defects and impurities in perovskite material. Lastly, we have discussed the various physical and chemical defect passivation techniques for the bulk, grain boundaries and interface defect passivation in perovskite-based thin films solar cells. Various point defect passivation strategies such as incorporation of metal cations/anions, zwitterions, additives, Lewis acid and Lewis base are discussed briefly. Other strategies for the perovskite/contact interface defect passivation, antisolvent vapor-assisted crystallization and thin film optimization are also summarized. Based on our study, currently the defect detection and defect passivation in perovskite semiconductor are highly challenging tasks and require a range of experimental techniques and experimental defect passivation strategies, but in terms of increasing the photovoltaic performance of perovskite solar cell these exercises are observed to be highly fruitful. Detailed study of bulk defect and surface defect contribution is also absolutely critical for the further enhancement of the power conversion efficiency in perovskite solar cell after the initial surge. The linkage between the kinetics of defect formation and stability of perovskite material is still a gray area. Majority of studies discussed in the review are based on archetypal perovskite which contains complicated interaction between organic and inorganic constitute at atomic scales, and there is no reason to believe that pure inorganic-based perovskite will also behave the same way as the hybrid perovskite. So, the defect study related to the other novel perovskite-based semiconductor still demands further attention since various perovskite-based semiconductor offers different functionality of physical parameters of its own. In a nutshell, this review provides a comprehensive overview of the defect formation, defect recombination and defect mitigations strategies in perovskite-based semiconductor as well as perovskite-based solar cells.

Declarations

Conflict of interest The authors declare no competing interests.

References

1. A. Kojima, K. Teshima, Y. Shirai, T. Miyasaka, Organometal halide perovskites as visible-light sensitizers for photovoltaic cells. J. Am. Chem. Soc. **131**(17), 6050–6051 (2009). https://doi.org/10.1021/ja809598r

2. M. Jeong, I.W. Choi, E.M. Go, Y. Cho, M. Kim, B. Lee, S. Jeong, Y. Jo, H.W. Choi, J. Lee, J.-H. Bae, S.K. Kwak, D.S. Kim, C. Yang, Stable perovskite solar cells with efficiency exceeding 24.8% and 0.3-V voltage loss. Science **369**(6511), 1615 (2020). https://doi.org/10.1126/science.abb7167

3. M. Green, E. Dunlop, J. Hohl-Ebinger, M. Yoshita, N. Kopidakis, X. Hao, Solar cell efficiency tables (version 57). Prog. Photovoltaics Res. Appl. **29**(1), 3–15 (2020). https://doi.org/10.1002/pip.3371

4. S.D. Stranks, G.E. Eperon, G. Grancini, C. Menelaou, M.J.P. Alcocer, T. Leijtens, L.M. Herz, A. Petrozza, H.J. Snaith, Electron-hole diffusion lengths exceeding 1 micrometer in an organometal trihalide perovskite absorber. Science **342**(6156), 341 (2013). https://doi.org/10.1126/science.1243982

5. T. Singh, A. Kulkarni, M. Ikegami, T. Miyasaka, Effect of electron transporting layer on bismuth-based lead-free perovskite (CH3NH3)3 Bi2I9 for photovoltaic applications. ACS Appl. Mater. Interfaces. **8**(23), 14542–14547 (2016). https://doi.org/10.1021/acsami.6b02843

6. T. Singh, T. Miyasaka, High performance perovskite solar cell via multi-cycle low temperature processing of lead acetate precursor solutions. Chem. Commun. **52**(26), 4784–4787 (2016). https://doi.org/10.1039/C5CC10608G

7. T. Singh, M. Ikegami, T. Miyasaka, Ambient fabrication of 126 µm thick complete perovskite photovoltaic device for high flexibility and performance. ACS Applied Energy Materials. **1**(12), 6741–6747 (2018). https://doi.org/10.1021/acsaem.8b01623

8. W. Shockley, H.J. Queisser, Detailed balance limit of efficiency of p-n junction solar cells. J. Appl. Phys. **32**(3), 510–519 (1961). https://doi.org/10.1063/1.1736034

9. M.I. Hossain, W. Qarony, S. Ma, L. Zeng, D. Knipp, Y.H. Tsang, Perovskite/silicon tandem solar cells: From detailed balance limit calculations to photon management. Nano-Micro Letters **11**(1), 58 (2019). https://doi.org/10.1007/s40820-019-0287-8

10. Z. Wang, Z. Song, Y. Yan, S. Liu, and D. Yang, Perovskite—A perfect top cell for tandem devices to break the S–Q limit. Advanced Science. **6**, (7), pp. 1801704 (2019). https://doi.org/10.1002/advs.201801704.

11. D. König, K. Casalenuovo, Y. Takeda, G. Conibeer, J.F. Guillemoles, R. Patterson, L.M. Huang, M.A. Green, Hot carrier solar cells: Principles, materials and design. Phys. E. **42**(10), 2862–2866 (2010). https://doi.org/10.1016/j.physe.2009.12.032

12. T. Unold and L. Gütay, Photoluminescence analysis of thin-film solar cells, in advanced characterization techniques for thin film solar cells. p. 151–175 https://doi.org/10.1002/9783527636280.ch7.

13. R.L. Milot, G.E. Eperon, H.J. Snaith, M.B. Johnston, L.M. Herz, Temperature-dependent charge-carrier dynamics in CH3NH3PbI3 perovskite thin films. Adv Func Mater **25**(39), 6218–6227 (2015). https://doi.org/10.1002/adfm.201502340

14. W. Shockley, W.T. Read, Statistics of the recombinations of holes and electrons. Phys. Rev. **87**(5), 835–842 (1952). https://doi.org/10.1103/PhysRev.87.835

15. D.W. deQuilettes, K. Frohna, D. Emin, T. Kirchartz, V. Bulovic, D.S. Ginger, S.D. Stranks, Charge-carrier recombination in halide perovskites. Chem. Rev. **119**(20), 11007–11019 (2019). https://doi.org/10.1021/acs.chemrev.9b00169

16. A.A.B. Baloch, F.H. Alharbi, G. Grancini, M.I. Hossain, M.K. Nazeeruddin, N. Tabet, Analysis of photocarrier dynamics at interfaces in perovskite solar cells by time-resolved photoluminescence. The Journal of Physical Chemistry C. **122**(47), 26805–26815 (2018). https://doi.org/10.1021/acs.jpcc.8b07069

17. S.M. Sze, K.K. Ng, *Physics of Semiconductor Devices* (Wiley-Interscience, Hoboken, 2007)

18. T. Kirchartz, F. Staub, U. Rau, Impact of photon recycling on the open-circuit voltage of metal halide perovskite solar cells. ACS Energy Lett. **1**(4), 731–739 (2016). https://doi.org/10.1021/acsenergylett.6b00223

19. K. Tvingstedt, O. Malinkiewicz, A. Baumann, C. Deibel, H.J. Snaith, V. Dyakonov, H.J. Bolink, Radiative efficiency of lead iodide based perovskite solar cells. Sci Rep. **4**, 6071 (2014). https://doi.org/10.1038/srep06071

20. M.B. Johnston, L.M. Herz, Hybrid perovskites for photovoltaics: Charge-carrier recombination, diffusion, and radiative efficiencies. Acc Chem Res. **49**(1), 146–154 (2016). https://doi.org/10.1021/acs.accounts.5b00411

21 M.J. Trimpl, A.D. Wright, K. Schutt, L.R.V. Buizza, Z. Wang, M.B. Johnston, H.J. Snaith, P. Müller-Buschbaum, L.M. Herz, Charge-carrier trapping and radiative recombination in metal halide perovskite semiconductors. Adv. Func. Mater. **30**(42), 2004312 (2020). https://doi.org/10.1002/adfm.202004312

22. J. Chantana, Y. Kawano, T. Nishimura, A. Mavlonov, Q. Shen, K. Yoshino, S. Iikubo, S. Hayase, T. Minemoto, Impact of Auger recombination on performance limitation of perovskite solar cell. Sol. Energy **217**, 342–353 (2021). https://doi.org/10.1016/j.solener.2021.02.018

23. F. Staub, U. Rau, T. Kirchartz, Statistics of the Auger recombination of electrons and holes via defect levels in the band gap-application to lead-halide perovskites. ACS Omega **3**(7), 8009–8016 (2018). https://doi.org/10.1021/acsomega.8b00962

24. M. Jaraiz, L. Pelaz, E. Rubio, J. Barbolla, G.H. Gilmer, D.J. Eaglesham, H.J. Gossmann, J.M. Poate, Atomistic modeling of point and extended defects in crystalline materials. MRS Online Proc. Libr. **532**(1), 43–53 (1998). https://doi.org/10.1557/PROC-532-43

25. C.G. Van de Walle and A. Janotti, Advances in electronic structure methods for defects and impurities in solids, in Advanced calculations for defects in materials. p. 1–16 https://doi.org/10.1002/9783527638529.ch1.

26 H.I. Rasool, C. Ophus, A. Zettl, Atomic defects in two dimensional materials. Adv. Mater. **27**(38), 5771–5777 (2015). https://doi.org/10.1002/adma.201500231

27 J. Shim, E.-K. Lee, Y.J. Lee, R.M. Nieminen, Density-functional calculations of defect formation energies using supercell methods: Defects in diamond. Phys. Rev. B **71**(3), 035206 (2005). https://doi.org/10.1103/PhysRevB.71.035206

28. P. Xu, S. Chen, H.-J. Xiang, X.-G. Gong, S.-H. Wei, Influence of defects and synthesis conditions on the photovoltaic performance of perovskite semiconductor CsSnI3. Chem. Mater. **26**(20), 6068–6072 (2014). https://doi.org/10.1021/cm503122j

29 J.M. Ball, A. Petrozza, Defects in perovskite-halides and their effects in solar cells. Nat. Energy **1**(11), 16149 (2016). https://doi.org/10.1038/nenergy.2016.149

30 W.-J. Yin, T. Shi, Y. Yan, Unusual defect physics in CH3NH3PbI3 perovskite solar cell absorber. Appl. Phys. Lett. **104**(6), 063903 (2014). https://doi.org/10.1063/1.4864778

31. A. Buin, P. Pietsch, J. Xu, O. Voznyy, A.H. Ip, R. Comin, E.H. Sargent, Materials processing routes to trap-free halide perovskites. Nano Lett. **14**(11), 6281–6286 (2014). https://doi.org/10.1021/nl502612m

32. A. Walsh, D.O. Scanlon, S. Chen, X.G. Gong, S.-H. Wei, Self-regulation mechanism for charged point defects in hybrid halide perovskites. Angew. Chem. Int. Ed. **54**(6), 1791–1794 (2015). https://doi.org/10.1002/anie.201409740

33. C. Eames, J.M. Frost, P.R.F. Barnes, B.C. O'Regan, A. Walsh, M.S. Islam, Ionic transport in hybrid lead iodide perovskite solar cells. Nat. Commun. **6**(1), 7497 (2015). https://doi.org/10.1038/ncomms8497

34. H. Uratani, K. Yamashita, Charge carrier trapping at surface defects of perovskite solar cell absorbers: A first-principles study. The Journal of Physical Chemistry Letters. **8**(4), 742–746 (2017). https://doi.org/10.1021/acs.jpclett.7b00055

35. T. Li, X. Zhao, D. Yang, M.-H. Du, L. Zhang, Intrinsic defect properties in halide double perovskites for optoelectronic applications. Phys. Rev. Appl. **10**(4), 041001 (2018). https://doi.org/10.1103/PhysRevApplied.10.041001

36. K. Domanski, J.-P. Correa-Baena, N. Mine, M.K. Nazeeruddin, A. Abate, M. Saliba, W. Tress, A. Hagfeldt, M. Grätzel, Not all that glitters is gold: Metal-migration-induced degradation in perovskite solar cells. ACS Nano **10**(6), 6306–6314 (2016). https://doi.org/10.1021/acsnano.6b02613

37 M.A. Green, *Solar Cells: Operating Principles, Technology, and System Applications* (United States: Prentice-Hall Inc., Englewood Cliffs, 1982)

38. G.J. Wetzelaer, M. Scheepers, A.M. Sempere, C. Momblona, J. Avila, H.J. Bolink, Trap-assisted non-radiative recombination in organic-inorganic perovskite solar cells. Adv Mater. **27**(11), 1837–1841 (2015). https://doi.org/10.1002/adma.201405372

39. T. Singh, T. Miyasaka, Stabilizing the efficiency beyond 20% with a mixed cation perovskite solar cell fabricated in ambient air under controlled humidity. Adv. Energy Mater. **8**(3), 1700677 (2018). https://doi.org/10.1002/aenm.201700677

40. C.M. Wolff, P. Caprioglio, M. Stolterfoht, D. Neher, Nonradiative recombination in perovskite solar cells: The role of interfaces. Adv Mater **31**(52), e1902762 (2019). https://doi.org/10.1002/adma.201902762

41. J. Heath and P. Zabierowski, Capacitance spectroscopy of thin-film solar cells, in Advanced characterization techniques for thin film solar cells. p. 81–105 https://doi.org/10.1002/9783527636280.ch4.

42. T. Eisenbarth, T. Unold, R. Caballero, C.A. Kaufmann, H.-W. Schock, Interpretation of admittance, capacitance-voltage, and current-voltage signatures in Cu(In, Ga)Se2 thin film solar cells. J. Appl. Phys. **107**(3), 12 (2010). https://doi.org/10.1063/1.3277043

43. I.M. Dharmadasa, Y. Rahaq, A.A. Ojo, T.I. Alanazi, Perovskite solar cells: A deep analysis using current–voltage and capacitance–voltage techniques. J. Mater. Sci.: Mater. Electron. **30**(2), 1227–1235 (2018). https://doi.org/10.1007/s10854-018-0390-5

44. A. Guerrero, E.J. Juarez-Perez, J. Bisquert, I. Mora-Sero, G. Garcia-Belmonte, Electrical field profile and doping in planar lead halide perovskite solar cells. Appl. Phys. Lett. **105**(13), 6779 (2014). https://doi.org/10.1063/1.4896779

45. A. Guerrero, J. You, C. Aranda, Y.S. Kang, G. Garcia-Belmonte, H. Zhou, J. Bisquert, Y. Yang, Interfacial degradation of planar lead halide perovskite solar cells. ACS Nano **10**(1), 218–224 (2016). https://doi.org/10.1021/acsnano.5b03687

46. M. Samiee, S. Konduri, B. Ganapathy, R. Kottokkaran, H.A. Abbas, A. Kitahara, P. Joshi, L. Zhang, M. Noack, V. Dalal, Defect density and dielectric constant in perovskite solar cells. Appl Phys Lett **105**(15), 153502 (2014). https://doi.org/10.1063/1.4897329

47. O. Almora, I. Zarazua, E. Mas-Marza, I. Mora-Sero, J. Bisquert, G. Garcia-Belmonte, Capacitive dark currents, hysteresis, and electrode polarization in lead halide perovskite solar cells. The Journal of Physical Chemistry Letters. **6**(9), 1645–1652 (2015). https://doi.org/10.1021/acs.jpclett.5b00480

48. M. Fischer, K. Tvingstedt, A. Baumann, V. Dyakonov, Doping profile in planar hybrid perovskite solar cells identifying mobile ions. ACS Applied Energy Materials. **1**(10), 5129–5134 (2018). https://doi.org/10.1021/acsaem.8b01119

49. M.T. Khan, M. Salado, A. Almohammedi, S. Kazim, S. Ahmad, Elucidating the impact of charge selective contact in halide perovskite through impedance spectroscopy. Adv Mater Interf **6**(21), 1901193 (2019). https://doi.org/10.1002/admi.201901193

50. M. Salado, M. Andresini, P. Huang, M.T. Khan, F. Ciriaco, S. Kazim, S. Ahmad, Interface engineering by thiazolium iodide passivation towards reduced thermal diffusion and performance improvement in perovskite solar cells. Adv Func Mater **30**(14), 1910561 (2020). https://doi.org/10.1002/adfm.201910561

51. S. Reichert, J. Flemming, Q. An, Y. Vaynzof, J.-F. Pietschmann, C. Deibel, Ionic-defect distribution revealed by improved evaluation of deep-level transient spectroscopy on perovskite solar cells. Phys. Rev. Appl. **13**(3), 034018 (2020). https://doi.org/10.1103/PhysRevApplied.13.034018

52. S. Heo, G. Seo, Y. Lee, D. Lee, M. Seol, J. Lee, J.-B. Park, K. Kim, D.-J. Yun, Y.S. Kim, J.K. Shin, T.K. Ahn, M.K. Nazeeruddin, Deep level trapped defect analysis in CH3NH3PbI3 perovskite solar cells by deep level transient spectroscopy. Energy Environ. Sci. **10**(5), 1128–1133 (2017). https://doi.org/10.1039/c7ee00303j

53. A.Y. Polyakov, N.B. Smirnov, I.V. Shchemerov, D.S. Saranin, T.S. Le, S.I. Didenko, D.V. Kuznetsov, A. Agresti, S. Pescetelli, F. Matteocci, A. Di Carlo, Trap states in multication mesoscopic perovskite solar cells: A deep levels transient spectroscopy investigation. Appl. Phys. Lett. **113**(26), 263501 (2018). https://doi.org/10.1063/1.5053845

54. H.-C. Hsieh, C.-Y. Hsiow, K.-F. Lin, Y.-C. Shih, L. Wang, C. Renaud, T.-P. Nguyen, Analysis of defects and traps in N-I–P layered-structure of perovskite solar cells by charge-based deep level transient spectroscopy (Q-DLTS). The Journal of Physical Chemistry C. **122**(31), 17601–17611 (2018). https://doi.org/10.1021/acs.jpcc.8b01949

55. K. Xue, C. Renaud, P.Y. Chen, S.H. Yang, and T.P. Nguyen, Defect investigation in perovskite solar cells by the charge based deep level transient spectroscopy (Q-DLTS), in Advances in engineering research and application. p. 204–209 https://doi.org/10.1007/978-3-030-04792-4_28.

56 S. Reichert, Q. An, Y.W. Woo, A. Walsh, Y. Vaynzof, C. Deibel, Probing the ionic defect landscape in halide perovskite solar cells. Nat Commun. **11**(1), 6098 (2020). https://doi.org/10.1038/s41467-020-19769-8

57. M.H. Futscher, J.M. Lee, L. McGovern, L.A. Muscarella, T. Wang, M.I. Haider, A. Fakharuddin, L. Schmidt-Mende, B. Ehrler, Quantification of ion migration in CH3NH3PbI3 perovskite solar cells by transient capacitance measurements. Mater. Horiz. **6**(7), 1497–1503 (2019). https://doi.org/10.1039/C9MH00445A

58. D.B. Khadka, Y. Shirai, M. Yanagida, T. Masuda, K. Miyano, Enhancement in efficiency and optoelectronic quality of perovskite thin films annealed in MACl vapor. Sustainable Energy Fuels **1**(4), 755–766 (2017). https://doi.org/10.1039/C7SE00033B

59. J.W. Rosenberg, M.J. Legodi, Y. Rakita, D. Cahen, M. Diale, Laplace current deep level transient spectroscopy measurements of defect states in methylammonium lead bromide single crystals. J. Appl. Phys. **122**(14), 145701 (2017). https://doi.org/10.1063/1.4995970

60. W.S. Yang, B.W. Park, E.H. Jung, N.J. Jeon, Y.C. Kim, D.U. Lee, S.S. Shin, J. Seo, E.K. Kim, J.H. Noh, S.I. Seok, Iodide management in formamidinium-lead-halide-based perovskite layers for efficient solar cells. Science **356**(6345), 1376–1379 (2017). https://doi.org/10.1126/science.aan2301

61. H.-S. Duan, H. Zhou, Q. Chen, P. Sun, S. Luo, T.-B. Song, B. Bob, Y. Yang, The identification and characterization of defect states in hybrid organic–inorganic perovskite photovoltaics.

Phys. Chem. Chem. Phys. **17**(1), 112–116 (2015). https://doi.org/10.1039/C4CP04479G

62. G. Gordillo, C.A. Otálora, M.A. Reinoso, Trap center study in hybrid organic-inorganic perovskite using thermally stimulated current (TSC) analysis. J. Appl. Phys. **122**(7), 075304 (2017). https://doi.org/10.1063/1.4999297

63. J.L. Pautrat, B. Katircioglu, N. Magnea, D. Bensahel, J.C. Pfister, L. Revoil, Admittance spectroscopy: A powerful characterization technique for semiconductor crystals—Application to ZnTe. Solid-State Electron. **23**(11), 1159–1169 (1980). https://doi.org/10.1016/0038-1101(80)90028-3

64. M.T. Khan, P. Huang, A. Almohammedi, S. Kazim, S. Ahmad, Mechanistic origin and unlocking of negative capacitance in perovskites solar cells. iScience. **24**(2), 102024 (2021). https://doi.org/10.1016/j.isci.2020.102024

65. M. Taukeer Khan, A. Almohammedi, S. Kazim, S. Ahmad, Electrical methods to elucidate charge transport in hybrid perovskites thin films and devices. Chem Rec **20**(5), 452–465 (2020). https://doi.org/10.1002/tcr.201900055

66. Z. Xiao, Q. Dong, C. Bi, Y. Shao, Y. Yuan, J. Huang, Solvent annealing of perovskite-induced crystal growth for photovoltaic-device efficiency enhancement. Adv Mater. **26**(37), 6503–6509 (2014). https://doi.org/10.1002/adma.201401685

67. T. Walter, R. Herberholz, C. Müller, H.W. Schock, Determination of defect distributions from admittance measurements and application to Cu(In, Ga)Se2 based heterojunctions. J. Appl. Phys. **80**(8), 4411–4420 (1996). https://doi.org/10.1063/1.363401

68. J. Wu, J. Shi, Y. Li, H. Li, H. Wu, Y. Luo, D. Li, Q. Meng, Quantifying the interface defect for the stability origin of perovskite solar cells. Adv. Energy Mater. **9**(37), 1901352 (2019). https://doi.org/10.1002/aenm.201901352

69. R.A. Awni, Z. Song, C. Chen, C. Li, C. Wang, M.A. Razooqi, L. Chen, X. Wang, R.J. Ellingson, J.V. Li, Y. Yan, Influence of charge transport layers on capacitance measured in halide perovskite solar cells. Joule. **4**(3), 644–657 (2020). https://doi.org/10.1016/j.joule.2020.01.012

70. S.H. Cho, J. Byeon, K. Jeong, J. Hwang, H. Lee, J. Jang, J. Lee, T. Kim, K. Kim, M. Choi, Y.S. Lee, Investigation of defect-tolerant perovskite solar cells with long-term stability via controlling the self-doping effect. Adv. Energy Mater. **11**(17), 2100555 (2021). https://doi.org/10.1002/aenm.202100555

71. F. Deschler, M. Price, S. Pathak, L.E. Klintberg, D.D. Jarausch, R. Higler, S. Huttner, T. Leijtens, S.D. Stranks, H.J. Snaith, M. Atature, R.T. Phillips, R.H. Friend, High photoluminescence efficiency and optically pumped lasing in solution-processed mixed halide perovskite semiconductors. J Phys Chem Lett. **5**(8), 1421–1426 (2014). https://doi.org/10.1021/jz5005285

72. C. Barugkin, J. Cong, T. Duong, S. Rahman, H.T. Nguyen, D. Macdonald, T.P. White, K.R. Catchpole, Ultralow absorption coefficient and temperature dependence of radiative recombination of CH3NH3PbI3 perovskite from photoluminescence. J Phys Chem Lett. **6**(5), 767–772 (2015). https://doi.org/10.1021/acs.jpclett.5b00044

73. Y. Yamada, T. Nakamura, M. Endo, A. Wakamiya, Y. Kanemitsu, Photocarrier recombination dynamics in perovskite CH3NH3PbI3 for solar cell applications. J Am Chem Soc. **136**(33), 11610–11613 (2014). https://doi.org/10.1021/ja506624n

74. F. Staub, H. Hempel, J.-C. Hebig, J. Mock, U.W. Paetzold, U. Rau, T. Unold, T. Kirchartz, Beyond bulk lifetimes: Insights into lead halide perovskite films from time-resolved photoluminescence. Phys. Rev. Appl. **6**(4), 044017 (2016). https://doi.org/10.1103/PhysRevApplied.6.044017

75. D. Luo, R. Su, W. Zhang, Q. Gong, R. Zhu, Minimizing nonradiative recombination losses in perovskite solar cells. Nat.

Rev. Mater. **5**(1), 44–60 (2019). https://doi.org/10.1038/s41578-019-0151-y

76. W. Tress, N. Marinova, O. Inganäs, M.K. Nazeeruddin, S.M. Zakeeruddin, M. Graetzel, Predicting the open-circuit voltage of CH3NH3PbI3 perovskite solar cells using electroluminescence and photovoltaic quantum efficiency spectra: The role of radiative and non-radiative recombination. Adv. Energy Mater. **5**(3), 1400812 (2015). https://doi.org/10.1002/aenm.201400812

77. K. Wu, A. Bera, C. Ma, Y. Du, Y. Yang, L. Li, T. Wu, Temperature-dependent excitonic photoluminescence of hybrid organometal halide perovskite films. Phys. Chem. Chem. Phys. **16**(41), 22476–22481 (2014). https://doi.org/10.1039/C4CP03573A

78. T. Kirchartz, U. Rau, Electroluminescence analysis of high efficiency Cu(In, Ga)Se2 solar cells. J Appl Phys **102**(10), 104510 (2007). https://doi.org/10.1063/1.2817959

79. U. Rau, Reciprocity relation between photovoltaic quantum efficiency and electroluminescent emission of solar cells. Phys. Rev. B **76**(8), 085303 (2007). https://doi.org/10.1103/PhysRevB.76.085303

80. M. Okano, M. Endo, A. Wakamiya, M. Yoshita, H. Akiyama, Y. Kanemitsu, Degradation mechanism of perovskite CH3NH3PbI3 diode devices studied by electroluminescence and photoluminescence imaging spectroscopy. Appl. Phys. Express **8**(10), 102302 (2015). https://doi.org/10.7567/apex.8.102302

81. I. Schnitzer, E. Yablonovitch, C. Caneau, T.J. Gmitter, Ultrahigh spontaneous emission quantum efficiency, 99.7% internally and 72% externally, from AlGaAs/GaAs/AlGaAs double heterostructures. Appl. Phys. Lett. **62**(2), 131–133 (1993). https://doi.org/10.1063/1.109348

82. T. Trupke, J. Zhao, A. Wang, R. Corkish, M.A. Green, Very efficient light emission from bulk crystalline silicon. Appl. Phys. Lett. **82**(18), 2996–2998 (2003). https://doi.org/10.1063/1.1572473

83. I.L. Braly, D.W. deQuilettes, L.M. Pazos-Outón, S. Burke, M.E. Ziffer, D.S. Ginger, H.W. Hillhouse, Hybrid perovskite films approaching the radiative limit with over 90% photoluminescence quantum efficiency. Nat. Photonics **12**(6), 355–361 (2018). https://doi.org/10.1038/s41566-018-0154-z

84. Z. Hameiri, A. Mahboubi Soufiani, M.K. Juhl, L. Jiang, F. Huang, Y.-B. Cheng, H. Kampwerth, J.W. Weber, M.A. Green, T. Trupke, Photoluminescence and electroluminescence imaging of perovskite solar cells. Prog. Photovoltaics Res. Appl. **23**(12), 1697–1705 (2015). https://doi.org/10.1002/pip.2716

85. P. Würfel, S. Finkbeiner, E. Daub, Generalized Planck's radiation law for luminescence via indirect transitions. Appl. Phys. A **60**(1), 67–70 (1995). https://doi.org/10.1007/BF01577615

86. T. Handa, D.M. Tex, A. Shimazaki, A. Wakamiya, Y. Kanemitsu, Charge injection mechanism at heterointerfaces in CH3NH3PbI3 perovskite solar cells revealed by simultaneous time-resolved photoluminescence and photocurrent measurements. The Journal of Physical Chemistry Letters. **8**(5), 954–960 (2017). https://doi.org/10.1021/acs.jpclett.6b02847

87. M.B. Johnston, L.M. Herz, Hybrid perovskites for photovoltaics: Charge-carrier recombination, diffusion, and radiative efficiencies. Acc. Chem. Res. **49**(1), 146–154 (2016). https://doi.org/10.1021/acs.accounts.5b00411

88. A. Marchioro, J. Teuscher, D. Friedrich, M. Kunst, R. van de Krol, T. Moehl, M. Grätzel, J.-E. Moser, Unravelling the mechanism of photoinduced charge transfer processes in lead iodide perovskite solar cells. Nat. Photonics **8**(3), 250–255 (2014). https://doi.org/10.1038/nphoton.2013.374

89. T. Kirchartz, J.A. Márquez, M. Stolterfoht, T. Unold, Photoluminescence-based characterization of halide perovskites for photovoltaics. Adv. Energy Mater. **10**(26), 1904134 (2020). https://doi.org/10.1002/aenm.201904134

90. M. Stolterfoht, V.M. Le Corre, M. Feuerstein, P. Caprioglio, L.J.A. Koster, D. Neher, Voltage-dependent photoluminescence and how it correlates with the fill factor and open-circuit voltage in perovskite solar cells. ACS Energy Lett. **4**(12), 2887–2892 (2019). https://doi.org/10.1021/acsenergylett.9b02262

91. M. Rai, L.H. Wong, L. Etgar, Effect of perovskite thickness on electroluminescence and solar cell conversion efficiency. J Phys Chem Lett. **11**(19), 8189–8194 (2020). https://doi.org/10.1021/acs.jpclett.0c02363

92. G. Xing, B. Wu, X. Wu, M. Li, B. Du, Q. Wei, J. Guo, E.K. Yeow, T.C. Sum, W. Huang, Transcending the slow bimolecular recombination in lead-halide perovskites for electroluminescence. Nat Commun. **8**, 14558 (2017). https://doi.org/10.1038/ncomms14558

93. X. Yu, T. Liu, Q. Wei, C. Liang, K. Wang, J. Guo, D. Zhao, B. Wang, R. Chen, G. Xing, Tailoring the surface morphology and phase distribution for efficient perovskite electroluminescence. J Phys Chem Lett. **11**(15), 5877–5882 (2020). https://doi.org/10.1021/acs.jpclett.0c01252

94. X.-K. Liu, W. Xu, S. Bai, Y. Jin, J. Wang, R.H. Friend, F. Gao, Metal halide perovskites for light-emitting diodes. Nat. Mater. **20**(1), 10–21 (2021). https://doi.org/10.1038/s41563-020-0784-7

95. Y. Zou, Z. Yuan, S. Bai, F. Gao, B. Sun, Recent progress toward perovskite light-emitting diodes with enhanced spectral and operational stability. Materials Today Nano. **5**, 100028 (2019). https://doi.org/10.1016/j.mtnano.2019.100028

96. T. Kirchartz, J.A. Márquez, M. Stolterfoht, T. Unold, Photoluminescence-based characterization of halide perovskites for photovoltaics. Adv. Energy Mater. **10**(26), 4134 (2020). https://doi.org/10.1002/aenm.201904134

97. M. Karakus, S.A. Jensen, F. D'Angelo, D. Turchinovich, M. Bonn, E. Cánovas, Phonon–electron scattering limits free charge mobility in methylammonium lead iodide perovskites. The Journal of Physical Chemistry Letters. **6**(24), 4991–4996 (2015). https://doi.org/10.1021/acs.jpclett.5b02485

98. L.M. Herz, Charge-carrier mobilities in metal halide perovskites: Fundamental mechanisms and limits. ACS Energy Lett. **2**(7), 1539–1548 (2017). https://doi.org/10.1021/acsenergylett.7b00276

99. C. Wehrenfennig, M. Liu, H.J. Snaith, M.B. Johnston, L.M. Herz, Charge-carrier dynamics in vapour-deposited films of the organolead halide perovskite CH3NH3PbI3−xClx. Energy Environ. Sci. **7**(7), 2269–2275 (2014). https://doi.org/10.1039/c4ee01358a

100. R. Ulbricht, E. Hendry, J. Shan, T.F. Heinz, M. Bonn, Carrier dynamics in semiconductors studied with time-resolved terahertz spectroscopy. Rev. Mod. Phys. **83**(2), 543–586 (2011). https://doi.org/10.1103/RevModPhys.83.543

101. L. Wang, C. McCleese, A. Kovalsky, Y. Zhao, C. Burda, Femtosecond time-resolved transient absorption spectroscopy of CH3NH3PbI3 perovskite films: Evidence for passivation effect of PbI2. J Am Chem Soc. **136**(35), 12205–12208 (2014). https://doi.org/10.1021/ja504632z

102. C.-W. Chen, S.-Y. Hsiao, C.-Y. Chen, H.-W. Kang, Z.-Y. Huang, H.-W. Lin, Optical properties of organometal halide perovskite thin films and general device structure design rules for perovskite single and tandem solar cells. Journal of Materials Chemistry A. **3**(17), 9152–9159 (2015). https://doi.org/10.1039/C4TA05237D

103. J.M. Richter, M. Abdi-Jalebi, A. Sadhanala, M. Tabachnyk, J.P.H. Rivett, L.M. Pazos-Outón, K.C. Gödel, M. Price, F. Deschler, R.H. Friend, Enhancing photoluminescence yields in lead halide perovskites by photon recycling and light out-coupling. Nat. Commun. **7**(1), 13941 (2016). https://doi.org/10.1038/ncomms13941

104. F. Staub, T. Kirchartz, K. Bittkau, U. Rau, Manipulating the net radiative recombination rate in lead halide perovskite films by modification of light outcoupling. J Phys Chem Lett. **8**(20), 5084–5090 (2017). https://doi.org/10.1021/acs.jpclett.7b02224

105. T. Etienne, E. Mosconi, F. De Angelis, Dynamical origin of the Rashba effect in organohalide lead perovskites: A key to suppressed carrier recombination in perovskite solar cells? J Phys Chem Lett. **7**(9), 1638–1645 (2016). https://doi.org/10.1021/acs.jpclett.6b00564

106. F. Zheng, L.Z. Tan, S. Liu, A.M. Rappe, Rashba spin-orbit coupling enhanced carrier lifetime in CH(3)NH(3)PbI(3). Nano Lett. **15**(12), 7794–7800 (2015). https://doi.org/10.1021/acs.nanolett.5b01854

107. D. Ghosh, E. Welch, A.J. Neukirch, A. Zakhidov, S. Tretiak, Polarons in halide perovskites: A perspective. J Phys Chem Lett. **11**(9), 3271–3286 (2020). https://doi.org/10.1021/acs.jpclett.0c00018

108. K. Miyata, T.L. Atallah, X.Y. Zhu, Lead halide perovskites: Crystal-liquid duality, phonon glass electron crystals, and large polaron formation. Sci. Adv. **3**(10), e1701469 (2017). https://doi.org/10.1126/sciadv.1701469

109. D.P. McMeekin, G. Sadoughi, W. Rehman, G.E. Eperon, M. Saliba, M.T. Hörantner, A. Haghighirad, N. Sakai, L. Korte, B. Rech, M.B. Johnston, L.M. Herz, H.J. Snaith, A mixed-cation lead mixed-halide perovskite absorber for tandem solar cells. Science **351**(6269), 151 (2016). https://doi.org/10.1126/science.aad5845

110. D. Ghosh, A.R. Smith, A.B. Walker, M.S. Islam, Mixed a-cation perovskites for solar cells: Atomic-scale insights into structural distortion, hydrogen bonding, and electronic properties. Chem. Mater. **30**(15), 5194–5204 (2018). https://doi.org/10.1021/acs.chemmater.8b01851

111. R.P. Feynman, Slow electrons in a polar crystal. Phys. Rev. **97**(3), 660–665 (1955). https://doi.org/10.1103/PhysRev.97.660

112. K. Miyata, D. Meggiolaro, M. T. Trinh, P. P. Joshi, E. Mosconi, S. C. Jones, F. De Angelis, X.-Y. Zhu, Large polarons in lead halide perovskites. Sci. Adv. **3**, e1701217 (2017). https://doi.org/10.1126/sciadv.1701217

113 C. Wehrenfennig, G.E. Eperon, M.B. Johnston, H.J. Snaith, L.M. Herz, High charge carrier mobilities and lifetimes in organolead trihalide perovskites. Adv Mater **26**(10), 1584–1589 (2014). https://doi.org/10.1002/adma.201305172

114. Y. Yang, M. Yang, Z. Li, R. Crisp, K. Zhu, M.C. Beard, Comparison of recombination dynamics in CH3NH3PbBr 3 and CH3NH3PbI3 perovskite films: Influence of exciton binding energy. J Phys Chem Lett. **6**(23), 4688–4692 (2015). https://doi.org/10.1021/acs.jpclett.5b02290

115. R.L. Milot, G.E. Eperon, H.J. Snaith, M.B. Johnston, L.M. Herz, Temperature-dependent charge-carrier dynamics in CH3NH3PbI3 perovskite thin films. Adv. Func. Mater. **25**(39), 6218–6227 (2015). https://doi.org/10.1002/adfm.201502340

116. R. Sheng, A. Ho-Baillie, S. Huang, S. Chen, X. Wen, X. Hao, M.A. Green, Methylammonium lead bromide perovskite-based solar cells by vapor-assisted deposition. J Phys Chem C **119**(7), 3545–3549 (2015). https://doi.org/10.1021/jp512936z

117. W. Rehman, R.L. Milot, G.E. Eperon, C. Wehrenfennig, J.L. Boland, H.J. Snaith, M.B. Johnston, L.M. Herz, Charge-carrier dynamics and mobilities in formamidinium lead mixed-halide perovskites. Adv Mater. **27**(48), 7938–7944 (2015). https://doi.org/10.1002/adma.201502969

118. C. Wehrenfennig, G.E. Eperon, M.B. Johnston, H.J. Snaith, L.M. Herz, High charge carrier mobilities and lifetimes in organolead trihalide perovskites. Adv Mater. **26**(10), 1584–1589 (2014). https://doi.org/10.1002/adma.201305172

119. N.K. Noel, S.D. Stranks, A. Abate, C. Wehrenfennig, S. Guarnera, A.-A. Haghighirad, A. Sadhanala, G.E. Eperon, S.K.

Pathak, M.B. Johnston, A. Petrozza, L.M. Herz, H.J. Snaith, Lead-free organic–inorganic tin halide perovskites for photovoltaic applications. Energy Environ. Sci. **7**(9), 3061–3068 (2014). https://doi.org/10.1039/C4EE01076K

120. W. Rehman, D.P. McMeekin, J.B. Patel, R.L. Milot, M.B. Johnston, H.J. Snaith, L.M. Herz, Photovoltaic mixed-cation lead mixed-halide perovskites: Links between crystallinity, photostability and electronic properties. Energy Environ. Sci. **10**(1), 361–369 (2017). https://doi.org/10.1039/C6EE03014A

121. D.-Y. Son, S.-G. Kim, J.-Y. Seo, S.-H. Lee, H. Shin, D. Lee, N.-G. Park, Universal approach toward hysteresis-free perovskite solar cell via defect engineering. J. Am. Chem. Soc. **140**(4), 1358–1364 (2018). https://doi.org/10.1021/jacs.7b10430

122. N. Li, S. Tao, Y. Chen, X. Niu, C.K. Onwudinanti, C. Hu, Z. Qiu, Z. Xu, G. Zheng, L. Wang, Y. Zhang, L. Li, H. Liu, Y. Lun, J. Hong, X. Wang, Y. Liu, H. Xie, Y. Gao, Y. Bai, S. Yang, G. Brocks, Q. Chen, H. Zhou, Cation and anion immobilization through chemical bonding enhancement with fluorides for stable halide perovskite solar cells. Nat. Energy **4**(5), 408–415 (2019). https://doi.org/10.1038/s41560-019-0382-6

123. S. Collavini, A. Cabrera-Espinoza, J.L. Delgado, Organic polymers as additives in perovskite solar cells. Macromolecules **54**(12), 5451–5463 (2021). https://doi.org/10.1021/acs.macromol.1c00665

124. X. Xiao, J. Dai, Y. Fang, J. Zhao, X. Zheng, S. Tang, P.N. Rudd, X.C. Zeng, J. Huang, Suppressed ion migration along the in-plane direction in layered perovskites. ACS Energy Lett. **3**(3), 684–688 (2018). https://doi.org/10.1021/acsenergylett.8b00047

125. X. Zheng, Y. Deng, B. Chen, H. Wei, X. Xiao, Y. Fang, Y. Lin, Z. Yu, Y. Liu, Q. Wang, J. Huang, Dual functions of crystallization control and defect passivation enabled by sulfonic zwitterions for stable and efficient perovskite solar cells. Adv Mater. **30**(52), 1803428 (2018). https://doi.org/10.1002/adma.201803428

126. M. Wang, H. Wang, W. Li, X. Hu, K. Sun, Z. Zang, Defect passivation using ultrathin PTAA layers for efficient and stable perovskite solar cells with a high fill factor and eliminated hysteresis. Journal of Materials Chemistry A. **7**(46), 26421–26428 (2019). https://doi.org/10.1039/C9TA08314F

127. Y. Tidhar, E. Edri, H. Weissman, D. Zohar, G. Hodes, D. Cahen, B. Rybtchinski, S. Kirmayer, Crystallization of methyl ammonium lead halide perovskites: Implications for photovoltaic applications. J. Am. Chem. Soc. **136**(38), 13249–13256 (2014). https://doi.org/10.1021/ja505556s

128. S. Lee, M.-C. Tang, R. Munir, D. Barrit, Y.-J. Kim, R. Kang, J.-M. Yun, D.-M. Smilgies, A. Amassian, D.-Y. Kim, In situ study of the film formation mechanism of organic–inorganic hybrid perovskite solar cells: Controlling the solvate phase using an additive system. Journal of Materials Chemistry A. **8**(16), 7695–7703 (2020). https://doi.org/10.1039/D0TA00048E

129. C. Zhang, H. Zhang, R. Wang, D. You, W. Wang, C. Xu, J. Dai, Exciton photoluminescence of CsPbBr 3@SiO2 quantum dots and its application as a phosphor material in light-emitting devices. Optical Materials Express. **10**(4), 1007–1017 (2020). https://doi.org/10.1364/OME.389847

130. S. Baek, J.W. Han, D. Vidyasagar, H. Cho, H.-H. Ha, D.H. Kim, Y.-W. Heo, S. Lee, Room-temperature-processed amorphous Sn-In-O electron transport layer for perovskite solar cells. Materials. **13**(1), 32 (2019). https://doi.org/10.3390/ma13010032

131. A. Maiti, S. Chatterjee, L. Peedikakkandy, A.J. Pal, Defects and their passivation in hybrid halide perovskites toward solar cell applications. Solar Rrl. **4**(12), 2000505 (2020). https://doi.org/10.1002/solr.202000505

132. X. Zhang, L. Li, Z. Sun, J. Luo, Rational chemical doping of metal halide perovskites. Chem. Soc. Rev. **48**(2), 517–539 (2019). https://doi.org/10.1039/C8CS00563J

133. J. Jiang, X. Yang, Y. Huang, M. Li, Q. Tao, M. Fei, H.L. Cai, F.M. Zhang, X.S. Wu, Improvement in solar cell efficiency based on the MAPbI3 films extracted by a mixed anti-solvent. Appl. Phys. Lett. **117**(20), 203901 (2020). https://doi.org/10.1063/5.0019360

134. B.W. Park, N. Kedem, M. Kulbak, D.Y. Lee, W.S. Yang, N.J. Jeon, J. Seo, G. Kim, K.J. Kim, T.J. Shin, G. Hodes, D. Cahen, S.I. Seok, Understanding how excess lead iodide precursor improves halide perovskite solar cell performance. Nat Commun. **9**(1), 3301 (2018). https://doi.org/10.1038/s41467-018-05583-w

135. M. Abdi-Jalebi, M. Pazoki, B. Philippe, M.I. Dar, M. Alsari, A. Sadhanala, G. Divitini, R. Imani, S. Lilliu, J. Kullgren, H. Rensmo, M. Grätzel, R.H. Friend, Dedoping of lead halide perovskites incorporating monovalent cations. ACS Nano **12**(7), 7301–7311 (2018). https://doi.org/10.1021/acsnano.8b03586

136. W. Li, R. Long, J. Tang, O.V. Prezhdo, Influence of defects on excited-state dynamics in lead halide perovskites: Time-domain ab initio studies. The Journal of Physical Chemistry Letters. **10**(13), 3788–3804 (2019). https://doi.org/10.1021/acs.jpclett.9b00641

137. J. Kim, C.-H. Chung, K.-H. Hong, Understanding of the formation of shallow level defects from the intrinsic defects of lead tri-halide perovskites. Phys. Chem. Chem. Phys. **18**(39), 27143–27147 (2016). https://doi.org/10.1039/C6CP02886A

138. X. Gong, L. Guan, H. Pan, Q. Sun, X. Zhao, H. Li, H. Pan, Y. Shen, Y. Shao, L. Sun, Z. Cui, L. Ding, M. Wang, Highly efficient perovskite solar cells via nickel passivation. Adv. Func. Mater. **28**(50), 1804286 (2018). https://doi.org/10.1002/adfm.201804286

139. M.I. Saidaminov, J. Kim, A. Jain, R. Quintero-Bermudez, H. Tan, G. Long, F. Tan, A. Johnston, Y. Zhao, O. Voznyy, E.H. Sargent, Suppression of atomic vacancies via incorporation of isovalent small ions to increase the stability of halide perovskite solar cells in ambient air. Nat. Energy **3**, 648 (2018). https://doi.org/10.1038/s41560-018-0192-2

140. N. Chen, T. Cai, W. Li, K. Hills-Kimball, H. Yang, M. Que, Y. Nagaoka, Z. Liu, D. Yang, A. Dong, C.-Y. Xu, R. Zia, O. Chen, Yb- and Mn-doped lead-free double perovskite Cs2AgBiX6 (X = Cl–, Br–) nanocrystals. ACS Appl. Mater. Interfaces. **11**(18), 16855–16863 (2019). https://doi.org/10.1021/acsami.9b02367

141. G. Liu, H. Zheng, L. Zhang, H. Xu, S. Xu, X. Xu, Z. Liang, X. Pan, Tailoring multifunctional passivation molecules with halogen functional groups for efficient and stable perovskite photovoltaics. Chem. Eng. J. **407**, 127204 (2021). https://doi.org/10.1016/j.cej.2020.127204

142. H. Tan, A. Jain, O. Voznyy, X. Lan, F.P. García de Arquer, J.Z. Fan, R. Quintero-Bermudez, M. Yuan, B. Zhang, Y. Zhao, F. Fan, P. Li, L.N. Quan, Y. Zhao, Z.-H. Lu, Z. Yang, S. Hoogland, E.H. Sargent, Efficient and stable solution-processed planar perovskite solar cells via contact passivation. Science **355**(6326), 722 (2017). https://doi.org/10.1126/science.aai9081

143 Y. Shao, Z. Xiao, C. Bi, Y. Yuan, J. Huang, Origin and elimination of photocurrent hysteresis by fullerene passivation in CH3NH3PbI3 planar heterojunction solar cells. Nat. Commun. **5**(1), 5784 (2014). https://doi.org/10.1038/ncomms6784

144. N.K. Noel, A. Abate, S.D. Stranks, E.S. Parrott, V.M. Burlakov, A. Goriely, H.J. Snaith, Enhanced photoluminescence and solar cell performance via Lewis base passivation of organic–inorganic lead halide perovskites. ACS Nano **8**(10), 9815–9821 (2014). https://doi.org/10.1021/nn5036476

145. N.K. Noel, B. Wenger, S.N. Habisreutinger, J.B. Patel, T. Crothers, Z. Wang, R.J. Nicholas, M.B. Johnston, L.M. Herz, H.J. Snaith, Highly crystalline methylammonium lead tribromide perovskite films for efficient photovoltaic devices. ACS Energy Lett. **3**(6), 1233–1240 (2018). https://doi.org/10.1021/acsenergylett.8b00509

146. J. Xu, A. Buin, A.H. Ip, W. Li, O. Voznyy, R. Comin, M. Yuan, S. Jeon, Z. Ning, J.J. McDowell, P. Kanjanaboos, J.-P. Sun, X. Lan, L.N. Quan, D.H. Kim, I.G. Hill, P. Maksymovych, E.H. Sargent, Perovskite–fullerene hybrid materials suppress hysteresis in planar diodes. Nat. Commun. **6**(1), 7081 (2015). https://doi.org/10.1038/ncomms8081

147. E. Castro, J. Murillo, O. Fernandez-Delgado, L. Echegoyen, Progress in fullerene-based hybrid perovskite solar cells. Journal of Materials Chemistry C. **6**(11), 2635–2651 (2018). https://doi.org/10.1039/C7TC04302C

148. D.W. deQuilettes, S. Koch, S. Burke, R.K. Paranji, A.J. Shropshire, M.E. Ziffer, D.S. Ginger, Photoluminescence lifetimes exceeding 8 µs and quantum yields exceeding 30% in hybrid perovskite thin films by ligand passivation. ACS Energy Lett. **1**(2), 438–444 (2016). https://doi.org/10.1021/acsenergylett.6b00236

149. W. Li, H. Dong, X. Guo, N. Li, J. Li, G. Niu, L. Wang, Graphene oxide as dual functional interface modifier for improving wettability and retarding recombination in hybrid perovskite solar cells. Journal of Materials Chemistry A. **2**(47), 20105–20111 (2014). https://doi.org/10.1039/C4TA05196C

150. M. Hadadian, J.-P. Correa-Baena, E.K. Goharshadi, A. Ummadisingu, J.-Y. Seo, J. Luo, S. Gholipour, S.M. Zakeeruddin, M. Saliba, A. Abate, M. Grätzel, A. Hagfeldt, Enhancing efficiency of perovskite solar cells via N-doped graphene: Crystal modification and surface passivation. Adv. Mater. **28**(39), 8681–8686 (2016). https://doi.org/10.1002/adma.201602785

151. S. Lee, J.H. Park, B.R. Lee, E.D. Jung, J.C. Yu, D. Di Nuzzo, R.H. Friend, M.H. Song, Amine-based passivating materials for enhanced optical properties and performance of organic–inorganic perovskites in light-emitting diodes. The Journal of Physical Chemistry Letters. **8**(8), 1784–1792 (2017). https://doi.org/10.1021/acs.jpclett.7b00372

152. A. Abate, M. Saliba, D.J. Hollman, S.D. Stranks, K. Wojciechowski, R. Avolio, G. Grancini, A. Petrozza, H.J. Snaith, Supramolecular halogen bond passivation of organic–inorganic halide perovskite solar cells. Nano Lett. **14**(6), 3247–3254 (2014). https://doi.org/10.1021/nl500627x

153. C.-H. Tsai, C.-M. Lin, C.-H. Kuei, Improving the performance of perovskite solar cells by adding 1,8-diiodooctane in the CH3NH3PbI3 perovskite layer. Sol. Energy **176**, 178–185 (2018). https://doi.org/10.1016/j.solener.2018.10.037

154. Y. Zhao, K. Zhu, CH3NH3Cl-assisted one-step solution growth of CH3NH3PbI3: structure, charge-carrier dynamics, and photovoltaic properties of perovskite solar cells. The Journal of Physical Chemistry C. **118**(18), 9412–9418 (2014). https://doi.org/10.1021/jp502696w

155. Q. Hu, W. Chen, W. Yang, Y. Li, Y. Zhou, B.W. Larson, J.C. Johnson, Y.-H. Lu, W. Zhong, J. Xu, L. Klivansky, C. Wang, M. Salmeron, A.B. Djurišić, F. Liu, Z. He, R. Zhu, T.P. Russell, Improving efficiency and stability of perovskite solar cells enabled by a near-infrared-absorbing moisture barrier. Joule. **4**(7), 1575–1593 (2020). https://doi.org/10.1016/j.joule.2020.06.007

156. T. Singh, S. Öz, A. Sasinska, R. Frohnhoven, S. Mathur, T. Miyasaka, Sulfate-assisted interfacial engineering for high yield and efficiency of triple cation perovskite solar cells with alkali-doped TiO$_2$ electron-transporting layers. Adv. Func. Mater. **28**(14), 1706287 (2018). https://doi.org/10.1002/adfm.201706287

157. T. Singh, Y. Udagawa, M. Ikegami, K. Kunugita, K. Ema, T. Miyasaka, Tuning of perovskite solar cell performance via low-temperature brookite scaffolds surface modifications. APL Mater. **5**(1), 016103 (2017). https://doi.org/10.1063/1.4973892

158. C.-C. Zhang, Z.-K. Wang, S. Yuan, R. Wang, M. Li, M.F. Jimoh, L.-S. Liao, Y. Yang, Polarized ferroelectric polymers for high-performance perovskite solar cells. Adv. Mater. **31**(30), 1902222 (2019). https://doi.org/10.1002/adma.201902222

159. H. Zhou, Q. Chen, G. Li, S. Luo, T.-B. Song, H.-S. Duan, Z. Hong, J. You, Y. Liu, Y. Yang, Interface engineering of highly efficient perovskite solar cells. Science **345**(6196), 542 (2014). https://doi.org/10.1126/science.1254050

160. J.J. Yoo, S. Wieghold, M.C. Sponseller, M.R. Chua, S.N. Bertram, N.T.P. Hartono, J.S. Tresback, E.C. Hansen, J.-P. Correa-Baena, V. Bulović, T. Buonassisi, S.S. Shin, M.G. Bawendi, An interface stabilized perovskite solar cell with high stabilized efficiency and low voltage loss. Energy Environ. Sci. **12**(7), 2192–2199 (2019). https://doi.org/10.1039/C9EE00751B

161. J. Peng, Y. Wu, W. Ye, D.A. Jacobs, H. Shen, X. Fu, Y. Wan, T. Duong, N. Wu, C. Barugkin, H.T. Nguyen, D. Zhong, J. Li, T. Lu, Y. Liu, M.N. Lockrey, K.J. Weber, K.R. Catchpole, T.P. White, Interface passivation using ultrathin polymer–fullerene films for high-efficiency perovskite solar cells with negligible hysteresis. Energy Environ. Sci. **10**(8), 1792–1800 (2017). https://doi.org/10.1039/C7EE01096F

162 S.-H. Turren-Cruz, A. Hagfeldt, M. Saliba, Methylammonium-free, high-performance, and stable perovskite solar cells on a planar architecture. Science **362**(6413), 449 (2018). https://doi.org/10.1126/science.aat3583

163. M. Stolterfoht, C.M. Wolff, J.A. Márquez, S. Zhang, C.J. Hages, D. Rothhardt, S. Albrecht, P.L. Burn, P. Meredith, T. Unold, D. Neher, Visualization and suppression of interfacial recombination for high-efficiency large-area pin perovskite solar cells. Nat. Energy **3**(10), 847–854 (2018). https://doi.org/10.1038/s41560-018-0219-8

164. A. Al-Ashouri, A. Magomedov, M. Roß, M. Jošt, M. Talaikis, G. Chistiakova, T. Bertram, J.A. Márquez, E. Köhnen, E. Kasparavičius, S. Levcenco, L. Gil-Escrig, C.J. Hages, R. Schlatmann, B. Rech, T. Malinauskas, T. Unold, C.A. Kaufmann, L. Korte, G. Niaura, V. Getautis, S. Albrecht, Conformal monolayer contacts with lossless interfaces for perovskite single junction and monolithic tandem solar cells. Energy Environ. Sci. **12**(11), 3356–3369 (2019). https://doi.org/10.1039/C9EE02268F

165. J. Seo, S. Park, Y. Chan Kim, N.J. Jeon, J.H. Noh, S.C. Yoon, S.I. Seok, Benefits of very thin PCBM and LiF layers for solution-processed p–i–n perovskite solar cells. Energy Environmental Science. **7**(8), 2642–2646 (2014). https://doi.org/10.1039/C4EE01216J

166. M.J. Jeong, K.M. Yeom, S.J. Kim, E.H. Jung, J.H. Noh, Spontaneous interface engineering for dopant-free poly(3-hexylthiophene) perovskite solar cells with efficiency over 24%. Energy Environ. Sci. **14**(4), 2419–2428 (2021). https://doi.org/10.1039/D0EE03312J

167. G. Lu, F. He, S. Pang, H. Yang, D. Chen, J. Chang, Z. Lin, J. Zhang, C. Zhang, A PCBM-modified TiO$_2$ blocking layer towards efficient perovskite solar cells. Int. J. Photoenergy **2017**, 2562968 (2017). https://doi.org/10.1155/2017/2562968

168. G.S. Han, H.S. Chung, B.J. Kim, D.H. Kim, J.W. Lee, B.S. Swain, K. Mahmood, J.S. Yoo, N.-G. Park, J.H. Lee, H.S. Jung, Retarding charge recombination in perovskite solar cells using ultrathin MgO-coated TiO2 nanoparticulate films. Journal of Materials Chemistry A. **3**(17), 9160–9164 (2015). https://doi.org/10.1039/C4TA03684K

169. S.-K. Huang, Y.-C. Wang, W.-C. Ke, Y.-T. Kao, N.-Z. She, J.-X. Li, C.-W. Luo, A. Yabushita, D.-Y. Wang, Y.J. Chang, K. Tsukagoshi, C.-W. Chen, Unravelling the origin of the photocarrier dynamics of fullerene-derivative passivation of SnO2 electron transporters in perovskite solar cells. Journal of Materials Chemistry A. **8**(44), 23607–23616 (2020). https://doi.org/10.1039/D0TA08752A

170. O. Fernandez-Delgado, P.S. Chandrasekhar, N. Cano-Sampaio, Z.C. Simon, A.R. Puente-Santiago, F. Liu, E. Castro, L. Echegoyen, The role of fullerene derivatives in perovskite solar cells:

Electron transporting or electron extraction layers? Journal of Materials Chemistry C **9**, 10759–10767 (2021). https://doi.org/10.1039/D0TC05903J

171. S. Ghosh, S. Mishra, T. Singh, Antisolvents in perovskite solar cells: Importance, issues, and alternatives. Adv. Mater. Interfaces **7**(18), 2000950 (2020). https://doi.org/10.1002/admi.202000950

172. Q. Shan, J. Li, J. Song, Y. Zou, L. Xu, J. Xue, Y. Dong, C. Huo, J. Chen, B. Han, H. Zeng, All-inorganic quantum-dot light-emitting diodes based on perovskite emitters with low turn-on voltage and high humidity stability. Journal of Materials Chemistry C. **5**(18), 4565–4570 (2017). https://doi.org/10.1039/C6TC05578H

173. J. Zhang, G. Hodes, Z. Jin, S. Liu, All-inorganic CsPbX3 perovskite solar cells: Progress and prospects. Angew. Chem. Int. Ed. **58**(44), 15596–15618 (2019). https://doi.org/10.1002/anie.201901081

174. C.-G. Wu, C.-H. Chiang, Z.-L. Tseng, M.K. Nazeeruddin, A. Hagfeldt, M. Grätzel, High efficiency stable inverted perovskite solar cells without current hysteresis. Energy Environ. Sci. **8**(9), 2725–2733 (2015). https://doi.org/10.1039/C5EE00645G

175. S. Kim, I. Jeong, C. Park, G. Kang, I.K. Han, W. Kim, M. Park, Morphology control of perovskite in green antisolvent system for MAPbI3-based solar cells with over 20% efficiency. Sol. Energy Mater. Sol. Cells **203**, 110197 (2019). https://doi.org/10.1016/j.solmat.2019.110197

176. H. Taherianfard, G.-W. Kim, M.M. Byranvand, K. Choi, G. Kang, H. Choi, F. Tajabadi, N. Taghavinia, T. Park, Effective management of nucleation and crystallization processes in perovskite formation via facile control of antisolvent temperature. ACS Applied Energy Materials. **3**(2), 1506–1514 (2020). https://doi.org/10.1021/acsaem.9b01916

177. H. Li, Y. Xia, C. Wang, G. Wang, Y. Chen, L. Guo, D. Luo, S. Wen, High-efficiency and stable perovskite solar cells prepared using chlorobenzene/acetonitrile antisolvent. ACS Appl. Mater. Interfaces. **11**(38), 34989–34996 (2019). https://doi.org/10.1021/acsami.9b12323

178. J. Liu, N. Li, J. Jia, J. Dong, Z. Qiu, S. Iqbal, B. Cao, Perovskite films grown with green mixed anti-solvent for highly efficient solar cells with enhanced stability. Sol. Energy **181**, 285–292 (2019). https://doi.org/10.1016/j.solener.2019.02.020

179. D. Shi, V. Adinolfi, R. Comin, M. Yuan, E. Alarousu, A. Buin, Y. Chen, S. Hoogland, A. Rothenberger, K. Katsiev, Y. Losovyj, X. Zhang, P.A. Dowben, O.F. Mohammed, E.H. Sargent, O.M. Bakr, Low trap-state density and long carrier diffusion in organolead trihalide perovskite single crystals. Science **347**(6221), 519 (2015). https://doi.org/10.1126/science.aaa2725

180. C. Dong, X. Han, Y. Zhao, J. Li, L. Chang, W. Zhao, A green anti-solvent process for high performance carbon-based CsPbI2Br all-inorganic perovskite solar cell. Solar RRL. **2**(9), 1800139 (2018). https://doi.org/10.1002/solr.201800139

181. D.S. Ahmed, B.K. Mohammed, M.K.A. Mohammed, Long-term stable and hysteresis-free planar perovskite solar cells using green antisolvent strategy. J. Mater. Sci. **56**(27), 15205–15214 (2021). https://doi.org/10.1007/s10853-021-06200-w

182. L. Wang, X. Wang, L.-L. Deng, S. Leng, X. Guo, C.-H. Tan, W.C.H. Choy, C.-C. Chen, The mechanism of universal green antisolvents for intermediate phase controlled high-efficiency formamidinium-based perovskite solar cells. Mater. Horiz. **7**(3), 934–942 (2020). https://doi.org/10.1039/C9MH01679A

183. D. Prochowicz, M.M. Tavakoli, A. Solanki, T.W. Goh, K. Pandey, T.C. Sum, M. Saliba, P. Yadav, Understanding the effect of chlorobenzene and isopropanol anti-solvent treatments on the recombination and interfacial charge accumulation in efficient planar perovskite solar cells. Journal of Materials Chemistry A. **6**(29), 14307–14314 (2018). https://doi.org/10.1039/C8TA03782E

184. M.H. Kumar, N. Yantara, S. Dharani, M. Graetzel, S. Mhaisalkar, P.P. Boix, N. Mathews, Flexible, low-temperature, solution processed ZnO-based perovskite solid state solar cells. Chem. Commun. **49**(94), 11089–11091 (2013). https://doi.org/10.1039/C3CC46534A

185. M. Liu, M.B. Johnston, H.J. Snaith, Efficient planar heterojunction perovskite solar cells by vapour deposition. Nature **501**(7467), 395–398 (2013). https://doi.org/10.1038/nature12509

186. R. Szostak, S. Sanchez, P.E. Marchezi, A.S. Marques, J.C. Silva, M.S. Holanda, A. Hagfeldt, H.C.N. Tolentino, A.F. Nogueira, Revealing the perovskite film formation using the gas quenching method by in situ GIWAXS: Morphology, properties, and device performance. Adv. Func. Mater. **31**(4), 2007473 (2021). https://doi.org/10.1002/adfm.202007473

187. T.-B. Song, Q. Chen, H. Zhou, C. Jiang, H.-H. Wang, Y. Yang, Y. Liu, J. You, Y. Yang, Perovskite solar cells: Film formation and properties. Journal of Materials Chemistry A. **3**(17), 9032–9050 (2015). https://doi.org/10.1039/C4TA05246C

188. C.C. Stoumpos, C.D. Malliakas, M.G. Kanatzidis, Semiconducting tin and lead iodide perovskites with organic cations: Phase transitions, high mobilities, and near-infrared photoluminescent properties. Inorg. Chem. **52**(15), 9019–9038 (2013). https://doi.org/10.1021/ic401215x

189. D. Liu, T.L. Kelly, Perovskite solar cells with a planar heterojunction structure prepared using room-temperature solution processing techniques. Nat. Photonics **8**(2), 133–138 (2014). https://doi.org/10.1038/nphoton.2013.342

190. S. Pang, H. Hu, J. Zhang, S. Lv, Y. Yu, F. Wei, T. Qin, H. Xu, Z. Liu, G. Cui, NH2CH=NH2PbI3: An alternative organolead iodide perovskite sensitizer for mesoscopic solar cells. Chem. Mater. **26**(3), 1485–1491 (2014). https://doi.org/10.1021/cm404006p

191. Z. Xiao, C. Bi, Y. Shao, Q. Dong, Q. Wang, Y. Yuan, C. Wang, Y. Gao, J. Huang, Efficient, high yield perovskite photovoltaic devices grown by interdiffusion of solution-processed precursor stacking layers. Energy Environ Sci **7**(8), 2619–2623 (2014). https://doi.org/10.1039/C4EE01138D

192. S. Yang, S. Chen, E. Mosconi, Y. Fang, X. Xiao, C. Wang, Y. Zhou, Z. Yu, J. Zhao, Y. Gao, F. De Angelis, J. Huang, Stabilizing halide perovskite surfaces for solar cell operation with wide-bandgap lead oxysalts. Science **365**(6452), 473 (2019). https://doi.org/10.1126/science.aax3294

193. P. Ferdowsi, E. Ochoa-Martinez, S.S. Alonso, U. Steiner, M. Saliba, Ultrathin polymeric films for interfacial passivation in wide band-gap perovskite solar cells. Sci. Rep. **10**(1), 22260 (2020). https://doi.org/10.1038/s41598-020-79348-1

194. Q. Jiang, Y. Zhao, X. Zhang, X. Yang, Y. Chen, Z. Chu, Q. Ye, X. Li, Z. Yin, J. You, Surface passivation of perovskite film for efficient solar cells. Nat. Photonics **13**(7), 460–466 (2019). https://doi.org/10.1038/s41566-019-0398-2

195. J. Schmidt, A. Merkle, R. Brendel, B. Hoex, M.C.M.V. de Sanden, W.M.M. Kessels, Surface passivation of high-efficiency silicon solar cells by atomic-layer-deposited Al2O3. Prog. Photovoltaics Res. Appl. **16**(6), 461–466 (2008). https://doi.org/10.1002/pip.823

196. R. Hezel, K. Jaeger, Low-temperature surface passivation of silicon for solar cells. J. Electrochem. Soc. **136**(2), 518–523 (1989). https://doi.org/10.1149/1.2096673

197. A.G. Aberle, Surface passivation of crystalline silicon solar cells: A review. Prog. Photovoltaics Res. Appl. **8**(5), 473–487 (2000). https://doi.org/10.1002/1099-159X(200009/10)8:5%3c473::AID-PIP337%3e3.0.CO;2-D

198. C.N. Eisler, M.T. Sheldon, and H.A. Atwater. Enhanced performance of small GaAs solar cells via edge and surface passivation. in 2012 38th IEEE

Photovoltaic Specialists Conference. (Year). https://doi.org/10.1109/PVSC.2012.6317756.

199. M.G. Mauk, S. Xu, D.J. Arent, R.P. Mertens, G. Borghs, Study of novel chemical surface passivation techniques on GaAs pn junction solar cells. Appl. Phys. Lett. **54**(3), 213–215 (1989). https://doi.org/10.1063/1.101012

200. Q. He, M. Worku, L. Xu, C. Zhou, S. Lteif, J.B. Schlenoff, B. Ma, Surface passivation of perovskite thin films by phosphonium halides for efficient and stable solar cells. Journal of Materials Chemistry A. **8**(4), 2039–2046 (2020). https://doi.org/10.1039/c9ta12597c

201. J. Cao, B. Wu, R. Chen, Y. Wu, Y. Hui, B.W. Mao, N. Zheng, Efficient, hysteresis-free, and stable perovskite solar cells with ZnO as electron-transport layer: Effect of surface passivation. Adv Mater. **30**(11), 1705596 (2018). https://doi.org/10.1002/adma.201705596

202. E. Jokar, C.-H. Chien, A. Fathi, M. Rameez, Y.-H. Chang, E.W.-G. Diau, Slow surface passivation and crystal relaxation with additives to improve device performance and durability for tin-based perovskite solar cells. Energy Environ. Sci. **11**(9), 2353–2362 (2018). https://doi.org/10.1039/c8ee00956b

203. Z. Li, J. Dong, C. Liu, J. Guo, L. Shen, W. Guo, Surface passivation of perovskite solar cells toward improved efficiency and stability. Nanomicro Lett. **11**(1), 50 (2019). https://doi.org/10.1007/s40820-019-0282-0

204. H. Choi, X. Liu, H.I. Kim, D. Kim, T. Park, S. Song, A facile surface passivation enables thermally stable and efficient planar perovskite solar cells using a novel IDTT-based small molecule additive. Adv. Energy Mater. **11**(16), 2003829 (2021). https://doi.org/10.1002/aenm.202003829

205. G. Grancini, C. Roldán-Carmona, I. Zimmermann, E. Mosconi, X. Lee, D. Martineau, S. Narbey, F. Oswald, F. De Angelis, M. Graetzel, M.K. Nazeeruddin, One-year stable perovskite solar cells by 2D/3D interface engineering. Nat. Commun. **8**(1), 15684 (2017). https://doi.org/10.1038/ncomms15684

206. D.S. Lee, J.S. Yun, J. Kim, A.M. Soufiani, S. Chen, Y. Cho, X. Deng, J. Seidel, S. Lim, S. Huang, A.W.Y. Ho-Baillie, Passivation of grain boundaries by phenethylammonium in formamidinium-methylammonium lead halide perovskite solar cells. ACS Energy Lett. **3**(3), 647–654 (2018). https://doi.org/10.1021/acsenergylett.8b00121

207. S. Wang, T. Sakurai, W. Wen, Y. Qi, Energy level alignment at interfaces in metal halide perovskite solar cells. Adv. Mater. Interfaces **5**(22), 1800260 (2018). https://doi.org/10.1002/admi.201800260

208. F. Hou, B. Shi, T. Li, C. Xin, Y. Ding, C. Wei, G. Wang, Y. Li, Y. Zhao, X. Zhang, Efficient and stable perovskite solar cell achieved with bifunctional interfacial layers. ACS Appl. Mater. Interfaces. **11**(28), 25218–25226 (2019). https://doi.org/10.1021/acsami.9b06424

209. D. Yang, R. Yang, K. Wang, C. Wu, X. Zhu, J. Feng, X. Ren, G. Fang, S. Priya, S. Liu, High efficiency planar-type perovskite solar cells with negligible hysteresis using EDTA-complexed SnO2. Nat. Commun. **9**(1), 3239 (2018). https://doi.org/10.1038/s41467-018-05760-x

210. J. Liang, Z. Chen, G. Yang, H. Wang, F. Ye, C. Tao, G. Fang, Achieving high open-circuit voltage on planar perovskite solar cells via chlorine-doped tin oxide electron transport layers. ACS Appl. Mater. Interfaces. **11**(26), 23152–23159 (2019). https://doi.org/10.1021/acsami.9b03873

211. M. Abuhelaiqa, S. Paek, Y. Lee, K.T. Cho, S. Heo, E. Oveisi, A.J. Huckaba, H. Kanda, H. Kim, Y. Zhang, R. Humphry-Baker, S. Kinge, A.M. Asiri, M.K. Nazeeruddin, Stable perovskite solar cells using tin acetylacetonate based electron transporting layers. Energy Environ. Sci. **12**(6), 1910–1917 (2019). https://doi.org/10.1039/C9EE00453J

212. W. Chen, F.-Z. Liu, X.-Y. Feng, A.B. Djurišić, W.K. Chan, Z.-B. He, Cesium doped NiOx as an efficient hole extraction layer for inverted planar perovskite solar cells. Adv. Energy Mater. **7**(19), 1700722 (2017). https://doi.org/10.1002/aenm.201700722

213. W. Okada, T. Suga, K. Oyaizu, H. Segawa, H. Nishide, Perovskite/TiO2 interface passivation using poly(vinylcarbazole) and fullerene for the photovoltaic conversion efficiency of 21%. ACS Applied Energy Materials. **2**(4), 2848–2853 (2019). https://doi.org/10.1021/acsaem.9b00162

214. Y. Lee, S. Lee, G. Seo, S. Paek, K.T. Cho, A.J. Huckaba, M. Calizzi, D.-W. Choi, J.-S. Park, D. Lee, H.J. Lee, A.M. Asiri, M.K. Nazeeruddin, Efficient planar perovskite solar cells using passivated tin oxide as an electron transport layer. Advanced Science. **5**(6), 1800130 (2018). https://doi.org/10.1002/advs.201800130

215. H. Wang, Y. Zhao, Z. Wang, Y. Liu, Z. Zhao, G. Xu, T.-H. Han, J.-W. Lee, C. Chen, D. Bao, Y. Huang, Y. Duan, Y. Yang, Hermetic seal for perovskite solar cells: An improved plasma enhanced atomic layer deposition encapsulation. Nano Energy **69**, 104375 (2020). https://doi.org/10.1016/j.nanoen.2019.104375

216. S. Tan, I. Yavuz, N. De Marco, T. Huang, S.-J. Lee, C.S. Choi, M. Wang, S. Nuryyeva, R. Wang, Y. Zhao, H.-C. Wang, T.-H. Han, B. Dunn, Y. Huang, J.-W. Lee, Y. Yang, Steric impediment of ion migration contributes to improved operational stability of perovskite solar cells. Adv. Mater. **32**(11), 1906995 (2020). https://doi.org/10.1002/adma.201906995

217. Y. Zhao, P. Zhu, M. Wang, S. Huang, Z. Zhao, S. Tan, T.-H. Han, J.-W. Lee, T. Huang, R. Wang, J. Xue, D. Meng, Y. Huang, J. Marian, J. Zhu, Y. Yang, A Polymerization-assisted grain growth strategy for efficient and stable perovskite solar cells. Adv. Mater. **32**(17), 1907769 (2020). https://doi.org/10.1002/adma.201907769

218. J.-W. Lee, N.-G. Park, Chemical approaches for stabilizing perovskite solar cells. Adv. Energy Mater. **10**(1), 1903249 (2020). https://doi.org/10.1002/aenm.201903249

219. Y. Zhao, P. Zhu, S. Huang, S. Tan, M. Wang, R. Wang, J. Xue, T.-H. Han, S.-J. Lee, A. Zhang, T. Huang, P. Cheng, D. Meng, J.-W. Lee, J. Marian, J. Zhu, Y. Yang, Molecular interaction regulates the performance and longevity of defect passivation for metal halide perovskite solar cells. J. Am. Chem. Soc. **142**(47), 20071–20079 (2020). https://doi.org/10.1021/jacs.0c09560

220. F. Wang, M. Yang, S. Yang, X. Qu, L. Yang, L. Fan, J. Yang, F. Rosei, Iodine-assisted antisolvent engineering for stable perovskite solar cells with efficiency >21.3 %. Nano Energy **67**, 104224 (2020). https://doi.org/10.1016/j.nanoen.2019.104224

221. M. Abdi-Jalebi, M.I. Dar, A. Sadhanala, S.P. Senanayak, M. Grätzel, R.H. Friend, Monovalent cation doping of CH3NH3PbI3 for efficient perovskite solar cells. J. Vis. Exp. **121**, 55307 (2017). https://doi.org/10.3791/55307

222. M. Abdi-Jalebi, Z. Andaji-Garmaroudi, S. Cacovich, C. Stavrakas, B. Philippe, J.M. Richter, M. Alsari, E.P. Booker, E.M. Hutter, A.J. Pearson, S. Lilliu, T.J. Savenije, H. Rensmo, G. Divitini, C. Ducati, R.H. Friend, S.D. Stranks, Maximizing and stabilizing luminescence from halide perovskites with potassium passivation. Nature **555**(7697), 497–501 (2018). https://doi.org/10.1038/nature25989

223. X. Zheng, B. Chen, J. Dai, Y. Fang, Y. Bai, Y. Lin, H. Wei, X.C. Zeng, J. Huang, Nat. Energy **2**(7), 17102 (2017). https://doi.org/10.1038/nenergy.2017.102

224. S.M. Jain, Z. Qiu, L. Häggman, M. Mirmohades, M.B. Johansson, T. Edvinsson, G. Boschloo, Frustrated Lewis pair-mediated recrystallization of CH3NH3PbI3 for improved optoelectronic quality and high voltage planar perovskite solar cells. Energy Environ. Sci. **9**(12), 3770–3782 (2016). https://doi.org/10.1039/C6EE02544G

225. K. Chen, J. Wu, Y. Wang, Q. Guo, Q. Chen, T. Cao, X. Guo, Y. Zhou, N. Chen, M. Zhang, Y. Li, Defect passivation by alcohol-soluble small molecules for efficient p–i–n planar perovskite solar cells with high open-circuit voltage. Journal of Materials Chemistry A. **7**(37), 21140–21148 (2019). https://doi.org/10.1039/C9TA06718C

226. Y. Zhou, H. Zhong, J. Han, M. Tai, X. Yin, M. Zhang, Z. Wu, H. Lin, Synergistic effect of charge separation and defect passivation using zinc porphyrin dye incorporation for efficient and stable perovskite solar cells. Journal of Materials Chemistry A. **7**(46), 26334–26341 (2019). https://doi.org/10.1039/C9TA09369A

227. C. Liu, Z. Huang, X. Hu, X. Meng, L. Huang, J. Xiong, L. Tan, Y. Chen, Grain boundary modification via F4TCNQ to reduce defects of perovskite solar cells with excellent device performance. ACS Appl. Mater. Interfaces. **10**(2), 1909–1916 (2018). https://doi.org/10.1021/acsami.7b15031

228. G. Xu, R. Xue, W. Chen, J. Zhang, M. Zhang, H. Chen, C. Cui, H. Li, Y. Li, Y. Li, New strategy for two-step sequential deposition: Incorporation of hydrophilic fullerene in second precursor for high-performance p-i-n planar perovskite solar cells. Adv. Energy Mater. **8**(12), 1703054 (2018). https://doi.org/10.1002/aenm.201703054

229. W. Kong, T. Ding, G. Bi, H. Wu, Optical characterizations of the surface states in hybrid lead–halide perovskites. Phys. Chem. Chem. Phys. **18**(18), 12626–12632 (2016). https://doi.org/10.1039/C6CP00325G

230. Z. Xiao, Q. Dong, C. Bi, Y. Shao, Y. Yuan, J. Huang, Solvent annealing of perovskite-induced crystal growth for photovoltaic-device efficiency enhancement. Adv. Mater. **26**(37), 6503–6509 (2014). https://doi.org/10.1002/adma.201401685

231. X. Li, D. Bi, C. Yi, J.-D. Décoppet, J. Luo, S.M. Zakeeruddin, A. Hagfeldt, M. Grätzel, A vacuum flash–assisted solution process for high-efficiency large-area perovskite solar cells. Science **353**(6294), 58 (2016). https://doi.org/10.1126/science.aaf8060

232. V.M. Le Corre, E.A. Duijnstee, O. El Tambouli, J.M. Ball, H.J. Snaith, J. Lim, L.J.A. Koster, Revealing charge carrier mobility and defect densities in metal halide perovskites via space-charge-limited current measurements. ACS Energy Lett. **6**(3), 1087–1094 (2021). https://doi.org/10.1021/acsenergylett.0c02599

233. E.A. Duijnstee, J.M. Ball, V.M. Le Corre, L.J.A. Koster, H.J. Snaith, J. Lim, Toward understanding space-charge limited current measurements on metal halide perovskites. ACS Energy Lett. **5**(2), 376–384 (2020). https://doi.org/10.1021/acsenergylett.9b02720

234. V. Adinolfi, M. Yuan, R. Comin, E.S. Thibau, D. Shi, M.I. Saidaminov, P. Kanjanaboos, D. Kopilovic, S. Hoogland, Z.-H. Lu, O.M. Bakr, E.H. Sargent, The In-gap electronic state spectrum of methylammonium lead iodide single-crystal perovskites. Adv. Mater **28**(17), 3406–3410 (2016). https://doi.org/10.1002/adma.201505162

235. M. Abdi-Jalebi, M.I. Dar, A. Sadhanala, S.P. Senanayak, M. Franckevičius, N. Arora, Y. Hu, M.K. Nazeeruddin, S.M. Zakeeruddin, M. Grätzel, R.H. Friend, Impact of monovalent cation halide additives on the structural and optoelectronic properties of CH3NH3PbI3 perovskite. Adv Energy Mater **6**(10), 1502472 (2016). https://doi.org/10.1002/aenm.201502472

236. M.I. Saidaminov, A.L. Abdelhady, B. Murali, E. Alarousu, V.M. Burlakov, W. Peng, I. Dursun, L. Wang, Y. He, G. Maculan, A. Goriely, T. Wu, O.F. Mohammed, O.M. Bakr, High-quality bulk hybrid perovskite single crystals within minutes by inverse temperature crystallization. Nat. Commun. **6**(1), 7586 (2015). https://doi.org/10.1038/ncomms8586

237. B.-W. Park, N. Kedem, M. Kulbak, D.Y. Lee, W.S. Yang, N.J. Jeon, J. Seo, G. Kim, K.J. Kim, T.J. Shin, G. Hodes, D. Cahen, S.I. Seok, Understanding how excess lead iodide precursor improves halide perovskite solar cell performance. Nat. Commun. **9**(1), 3301 (2018). https://doi.org/10.1038/s41467-018-05583-w

238. M. Zhang, Q. Chen, R. Xue, Y. Zhan, C. Wang, J. Lai, J. Yang, H. Lin, J. Yao, Y. Li, L. Chen, Y. Li, Reconfiguration of interfacial energy band structure for high-performance inverted structure perovskite solar cells. Nat. Commun. **10**(1), 4593 (2019). https://doi.org/10.1038/s41467-019-12613-8

239. T.-Y. Yang, G. Gregori, N. Pellet, M. Grätzel, J. Maier, The significance of ion conduction in a hybrid organic–inorganic lead-iodide-based perovskite photosensitizer. Angew. Chem. Int. Ed. **54**(27), 7905–7910 (2015). https://doi.org/10.1002/anie.201500014

240. J. Dhar, S. Sil, A. Dey, P.P. Ray, D. Sanyal, Positron annihilation spectroscopic investigation on the origin of temperature-dependent electrical response in methylammonium lead iodide perovskite. The Journal of Physical Chemistry Letters. **8**(8), 1745–1751 (2017). https://doi.org/10.1021/acs.jpclett.7b00446